On the Conservatisms of Nepheline Predictors for Canister Centreline Cooled (CCC) High-Level Waste (HLW) Glasses

CORNWALL, Jack D. <http://orcid.org/0009-0004-3651-2216>, BELL, Anthony <http://orcid.org/0000-0001-5038-5621>, SCRIMSHIRE, Alex <http://orcid.org/0000-0002-6828-3620>, SMITH, Robin <http://orcid.org/0000-0002-9671-8599>, FILLEUL, Axandre, SARGIN, Irmak, KRUGER, Albert A and BINGHAM, Paul <http://orcid.org/0000-0001-6017-0798>

International Journal of Applied Glass Science

RESEARCH ARTICLE OPEN ACCESS

On the Conservatisms of Nepheline Predictors for Canister Centerline Cooled (CCC) High-Level Waste (HLW) Glasses

Jack D. Cornwall[1] | Anthony M. T. Bell[1] | Alex Scrimshire[1] | Robin Smith[1] | Axandre Filleul[1] | Irmak Sargin[2] | Albert A. Kruger[3] | Paul A. Bingham[1]

[1]School of Engineering and Built Environment, Sheffield Hallam University, Sheffield, UK | [2]Department of Metallurgical and Materials Engineering, Middle East Technical University (METU), Ankara, Turkiye | [3]US Department of Energy, Hanford Field Office, Richland, Washington, USA

Correspondence: Jack D. Cornwall (j.cornwall@shu.ac.uk)

Received: 23 December 2025 | **Revised:** 28 March 2026 | **Accepted:** 28 April 2026

Keywords: CCC | crystallization | HLW | KE1 | nepheline | nuclear waste glass | PCT | sodium alumino-boro-silicate | XRD

ABSTRACT

Multiple models and feature sets have been generated, which attempt to predict the crystallization of nepheline ($NaAlSiO_4$) in high-level radioactive waste (HLW) glasses under canister centerline cooling (CCC) conditions. Earlier models were found to be overly conservative, while newer models had a not insignificant rate of false positives and negatives, with a drop off in predictive accuracy along the nepheline prediction boundary. Only partial or limited explanations for this drop in accuracy have hitherto been put forward, for example, experimental inaccuracies or insufficient data points. This research presents evidence consistent with a primary cause being differences in surface area to volume ratio (SA/V) between small experimental glass samples and large-scale canister glasses. Furthermore, a new simplified, simulated (non-radioactive) HLW glass composition (KE1) has been designed as a starting point for experiments that focus on the low accuracy region of nepheline predictor models, lying between compositions that are prone to precipitate nepheline and compositions that are not. This glass has been characterized using multiple techniques, and several experiments have been designed and implemented to highlight the marked effects of SA/V on the outcome of the product consistency test (PCT-B, ASTM C1285-21) used to validate the chemical durability (as measured by PCT tests) of nuclear waste glasses destined for geological disposal.

1 | Introduction

Borosilicate glass is the chief candidate among nuclear nations for use as the host matrix to immobilize high-level radioactive waste [1]. Borosilicate glass has benefits in both its processing parameters (good processability, manufacturability, can incorporate a wide range of components into its matrix, and relatively high waste loading is possible). Furthermore, the end product has many desirable qualities (acceptable chemical durability, resistance to radiation damage, and thermal stability) [2–5].

The Hanford Site in Washington State, USA, is home to over 200 million liters of nuclear waste, historically stored in 177 underground tanks [6]; the Department of Energy (DOE) plans to separate high-level waste (HLW), which represents ~5% of the waste volume but accounts for ~70% of the radioactivity [7], from the low activity waste (LAW). These will subsequently be mixed with glass-forming chemicals (GFC), forming the melter feeds which will then be fed directly into the melters at the vitrification plant in a direct-feed approach [8–10]. Many of the solids in the tanks are high in alumina; therefore, incoming direct-feed HLW (DFHLW) waste streams are expected to be high in Al [11]. The HLW can be further subdivided into six categories, delineated by statistical cluster analysis [12], separated by the glass formulation limiting oxide, the most plentiful of which is high-alumina (Al_2O_3) wastes [6].

Alumina and sodium oxide are two of the most plentiful oxides in Hanford waste due to the dissolved aluminum cladding (often dissolved using NaOH) and aluminum nitride used in the REDOX process [6]. The alumina-rich HLW and variants of it constitute approximately 50% of the Hanford HLW [6, 13], if not more, in the instance where DFHLW is employed. Furthermore, since Al and Na are often present simultaneously in waste streams, maximizing Al_2O_3 and Na_2O waste loading (as two of the most plentiful oxides) is desirable in order to limit: (i) the volume of glass processed as well as the accompanying energy requirements, (ii) the amount of raw GFCs needed, (iii) the volume of geological repository that will need to be excavated to accommodate the vitrified waste canisters, and (iv) the duration of the cleanup mission.

The limiting factor when it comes to the waste loading of high-alumina waste is its propensity to precipitate crystalline nepheline ($NaAlSiO_4$) in the slowest-cooled portion of the canister, where the kinetics and thermodynamics favor devitrification [14]. Nepheline is a crystal which itself is highly chemically durable [15], however, it tends to remove three moles of network former (SiO_2 and Al_2O_3) for each mole of network modifier (Na_2O) from the surrounding glass [16, 17], resulting in a chemically less durable glass adjacent to the nepheline, however it should be noted that Nepheline which precipitates from HLW melts can incorporate many other elements [18].

The matter is further complicated, however, as certain glass compositions that do precipitate measurable fractions of nepheline pass the DWPF EA comparative assessment [19]; while other glass compositions that do not precipitate nepheline either fail the DWPF EA comparative test or result in considerably lower chemical durability [20].

Furthermore, the glass and the crystal are likely to have different coefficients of thermal expansion, resulting in cracking and thus increased surface area exposed to potential aqueous leaching in a geological repository [21–27]. These two effects could, in combination, result in the waste package (whole canister) durability, as measured by a PCT test, performing orders of magnitude more poorly [13, 28]. These combined effects are difficult to model via lab-scale product consistency tests (PCT) [29], a dissolution test by which any glass composition earmarked for disposal must outperform the Defense Waste Processing Facility Environmental Assessment (DWPF EA) glass [30], the benchmark standard for minimal acceptable durability as set out in the acceptance criterion of the WAPS [31]. Alongside PCT, other tests such as the Materials Characterization Centre Protocol 1 (MCC-1) (ASTM C1220-21) [32], Vapor Hydration Test (VHT) (ASTM C1663-24) [33] and Toxicity Characteristic Leaching Procedure (TCLP) (EPA 1311) [34] are also often used to look at alteration layer, dissolution and chemical durability in nuanced ways, certain studies conduct more than one of these tests side by side [35, 36] on both quenched and heat-treated samples. This study, however, focuses on PCT-B.

Wastes are to be processed by being mixed with raw GFCs, usually in either oxide or carbonate form, before being melted inside a Monofrax-K3-lined Joule-heated ceramic melter (JHCM) [37]. The molten glass is then poured and allowed to cool and vitrify inside a 304L stainless steel canister.

The Hanford canisters have a diameter of 0.61m and a length of ~4.5m with a fill volume of 1.315m^3 [38–40], designed to be tall and narrow for more rapid heat loss, and the inside of the pour caves will be actively cooled with HVAC systems [41] to aid with cooling. Nevertheless, in highly waste-loaded glass compositions rich in Al_2O_3 and Na_2O, nepheline can precipitate, especially along the canister centerline, where cooling is slowest (furthest from the more rapidly cooled surface of the canister).

1.1 | Canister Centerline Cooled Nepheline Prediction Database and Models

In an effort to tackle the problems caused by the crystallization of nepheline, a database of slow-cooled laboratory-produced glasses and the resultant crystal fraction of nepheline and chemical durability (as measured by 7-day PCT tests using both A and B variants of the test) has been compiled over the past few decades. The cooling regime used is dubbed CCC and is deemed the scenario resulting in the greatest levels of nepheline devitrification, as measured along the canister centerline in experimental canister pours [42]. The CCC cooling regime is summarized in Table 1.

The nepheline database has since been used to generate models or "*nepheline predictors*" which based on compositional inputs, will attempt to determine whether or not a given glass composition will precipitate nepheline under CCC conditions. Four of these models, with increasing complexity, are briefly summarized below:

1.1.1 | Nepheline Discriminator (ND) Model

The first and simplest model, the nepheline discriminator (ND) model [16], attempts to ensure that sufficient SiO_2 is present in a glass to keep the composition away from the Nepheline phase field in the $SiO2\text{-}Al_2O_3\text{-}Na_2O$ ternary phase diagram. This is represented by a straight line at 0.62 weight fraction (wt. fr.) of SiO_2. This is shown in Figure 1.

The ND model states that nepheline is unlikely to precipitate when:

$$N_{si} = \frac{g_{SiO_2}}{g_{SiO_2} + g_{Al_2O_3} + g_{Na_2O}} > 0.62 \quad (1)$$

Equation (1)—**Nepheline discriminator**.

Where N_{Si} is the normalized silica wt. fr. g_{SiO_2}, $g_{Al_2O_3}$, and g_{Na_2O} are simply the wt. fr. of the respective oxide. While this model was deemed successful at limiting nepheline crystallization, it was found to be too conservative [45] as it limited Al_2O_3 loading to 18 wt% whereas compositions with 30 wt% loading had already been achieved [13, 46].

1.1.2 | ND and OB Quadrant (OB) Model

McCloy et al. [47] improved upon this model by combining the ND model with the calculated theoretical optical basicity (Λ_{glass}) of each glass, as results showed that adding acidic components

TABLE 1 | Canister centerline cooling (CCC) program used in this study, reproduced from [42], including 30 min hold at 1150°C, which is used to ensure no crystals or potential nucleation sites are present at the start of the CCC cooling procedure.

Segment	Segment start temp (°C)	Segment end temp (°C)	Rate (°C/h)	Rate (°C/min)	Segment time (h)	Segment time (min)	Segment description
1	RT	1150	300	5	3.767	226.000	Ramp
2	1150	1150	0	0	0.500	30.000	Hold
3	1150	1050	~4200	~70	0.033	2.000	Freefall
4	1050	980	−93.36	−1.556	0.750	44.987	Slow cool
5	980	930	−48.36	−0.806	1.034	62.035	Slow cool
6	930	875	−35.46	−0.591	1.551	93.063	Slow cool
7	875	825	−23.28	−0.388	2.148	128.866	Slow cool
8	825	775	−15.18	−0.253	3.294	197.628	Slow cool
9	775	725	−16.68	−0.278	2.998	179.856	Slow cool
10	725	400	−18.24	−0.304	17.818	1069.079	Slow cool

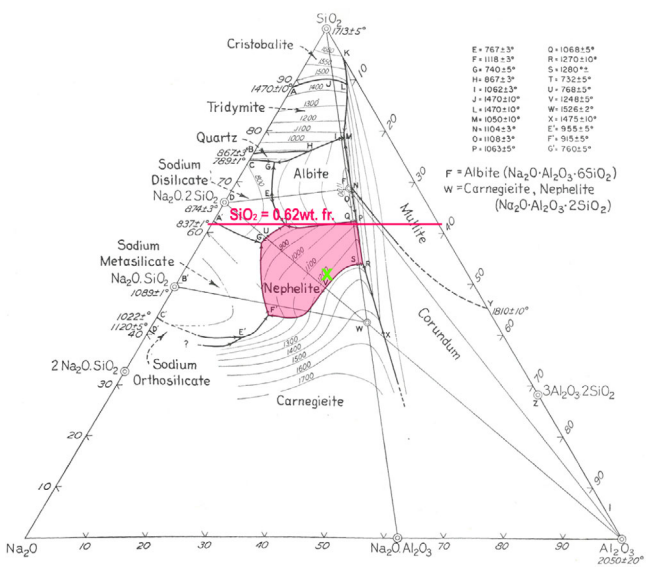

FIGURE 1 | Sodium oxide, silica, alumina ternary phase diagram, with nepheline (referred to as nephelite) phase field highlighted and nepheline discriminator (ND = 0.62) overlain. Adapted from Phase Diagrams for Ceramists (1956) [43] with permission of The American Ceramic Society. Original Source: Schairer and Bowen [44]. The normalized position of the KE1 composition within the Na_2O-Al_2O_3-SiO_2 space is marked with a green "X".

(SiO_2, B_2O_3, P_2O_5, etc.) and removing alkaline components (K_2O, Na_2O, etc.) correlated with the propensity of a given glass to precipitate nepheline. As a result of this work, a quadrant model was devised, shown in Figure 2.

The theoretical value of Λ_{glass} is given by Equation (2):

$$\Lambda_{glass} = \frac{\sum_i x_i q_i \Lambda_i}{\sum_i x_i q_i} \quad (2)$$

Equation (2)—**Theoretical optical basicity value** [47].

Where x_i is the i-th oxide mole fraction, q_i is the number of oxygen atoms in the i-th component oxide, and Λ_i is the i-th oxide molar basicity. The molar basicity of common glass-forming oxides can be found in the following reference [48].

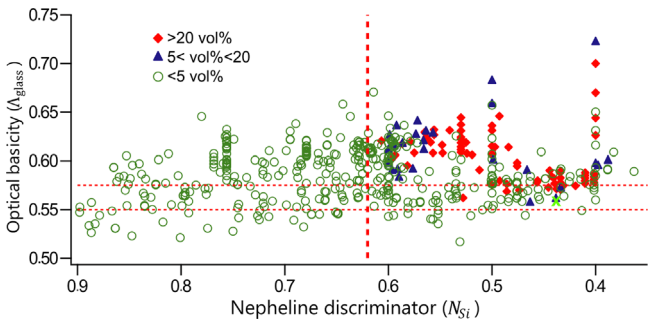

FIGURE 2 | Quadrant system which combines N_{Si} and Λ_{glass} to separate nepheline precipitating compositions. The location of the KE1 composition in this reduced feature space is marked with a green "X". Adapted with permission from McCloy et al. [47], John Wiley & Sons.

Glasses for which $N_{Si} < 0.62$ and $\Lambda_{glass} > 0.55/0.57$(upper right quadrant in Figure 2) were found to more accurately segregate compositions that precipitated nepheline, thus enabling an increase in the compositional space which could potentially be considered for vitrification. However, as can also be seen by the quadrant plot, many glasses that did not precipitate nepheline were also present in the top right quadrant and thus excluded by the model.

1.1.3 | Submixture Model (SM)

Vienna et al. [49] further worked to improve on the success of the ND model by adding more compositions to the database and attempting to incorporate the known effects of B_2O_3, P_2O_5, Li_2O, K_2O, CaO, MgO, and Fe_2O_3 (although it was found that P_2O_5, MgO, and Fe_2O_3 had little effect according to the SM model). A pseudo-ternary phase diagram was devised with corners represented by $A = Na_2O + 0.31CaO + 1.03Li_2O + 0.39K_2O$, $B = Al_2O_3$ and $C = SiO_2 + 1.74B_2O_3$ (for the optimized model), this is shown in Figure 3.

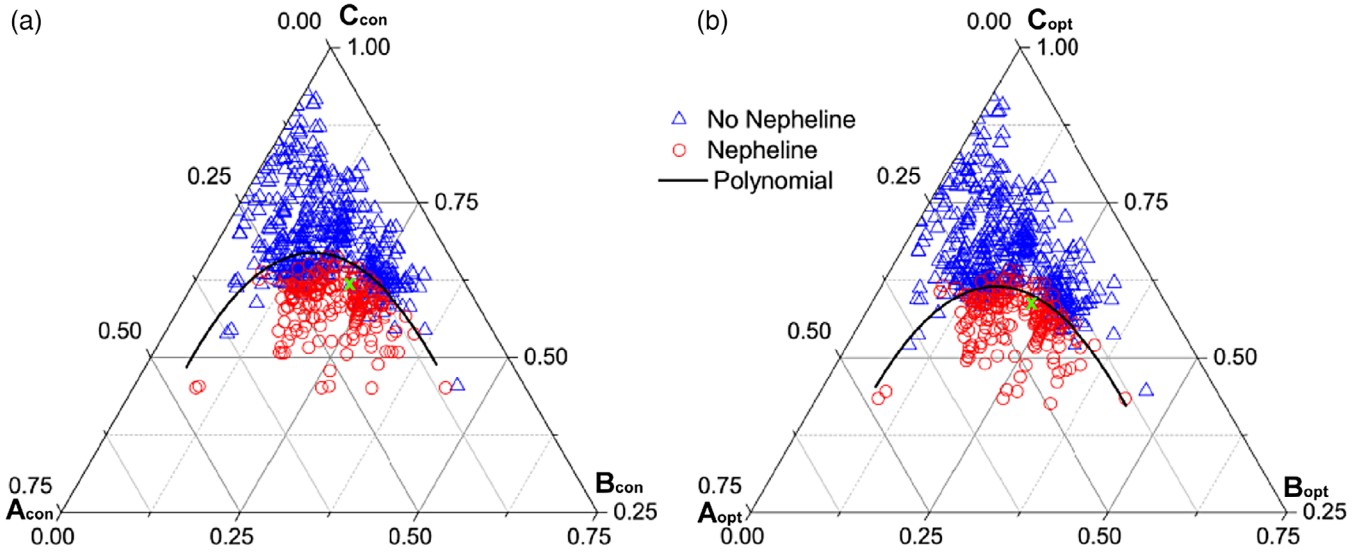

FIGURE 3 | (a) and (b) Conservative (left) and optimized (right) submixture models, which fit a polynomial through pseudo-ternary phase diagrams in an attempt to separate compositions that precipitate nepheline and those that do not. The optimized model tries to be as accurate as possible to increase waste loading, while the conservative model attempts to focus on reducing false positives. The location of the KE1 composition for both models is marked with a green "X". Adapted with permission from McCloy et al. [49], John Wiley & Sons.

A polynomial function was then fitted between the compositions of glasses that did and did not precipitate nepheline, as shown in Equation (3) below:

$$P = -\frac{bC + 2bB - \sqrt{3}C}{2(A + B + C)} - \frac{c(2B + C)^2}{4(A + B + C)^2} - a \qquad (3)$$

Equation (3)—**Submixture model** [49].

Where P is the polynomial represented by the black lines on the ternary plots in Figure 3a,b, which best separates the nepheline precipitating/non-precipitating space. Values of $P = 0$ find themselves on the black line, values of $P < 0$ (below the polynomial) fall in the regime where nepheline is predicted to crystallize, and values of $P > 0$ (above the polynomial) fall in the regime where no nepheline crystalization is predicted. A, B, and C are the corners of the pseudo ternary, which vary for the conservative and optimized model, and a, b, and c are fit constants that can be found in the original literature [49], these vary for the optimized and conservative fits. The SM model was found to increase maximum waste loading by up to 47% relative to ND and up to 12% relative to ND+OB, depending on waste stream, with 33% being the average improvement between ND and SM [49].

1.1.4 | Difference Based on Correlation (DC) Model

A more recent model dubbed "difference based on correlation" (DC) [50] is based on a linear summation of oxide contributions. This model has accuracy greater than or similar to previous models discussed, with a nepheline prediction accuracy of 92%, but importantly, has a more balanced rate of false negatives and false positives, allowing for higher waste loading. It was found that the model's accuracy was not consistent throughout the compositional space, and principal component (PC) analysis

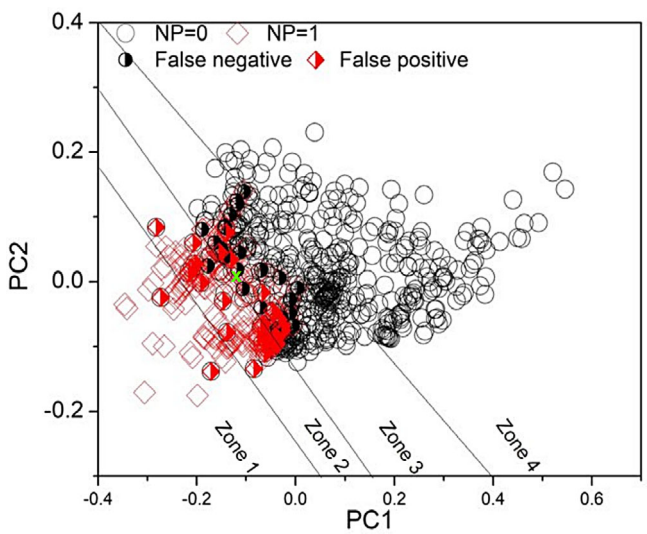

FIGURE 4 | Compositions from the nepheline database plotted in principal component space, showing lower accuracy zones 2 & 3 where most false positives and false negatives can be found [50]. The location of the KE1 composition is overlaid onto the plot, showing it is at the center of the low accuracy zone, and marked by a green "X". Adapted with permission from Sargin et al. [50], John Wiley & Sons.

allowed for the identification of zones of lower accuracy close to the hypersurface boundary (or knife edge) between compositions that did and did not precipitate nepheline, the PC space can be seen in Figure 4. The DC model is shown in Equation (4):

$$\begin{aligned} DC = &\left(g_{Al_2O_3} + g_{C_2O_3} + g_{P_2O_5} + g_{K_2O} + g_{Na_2O} + g_{Li_2O} + g_{Ti_2O}\right) \\ &- \left(g_{B_2O_3} + g_{Ce_2O_3} + g_{La_2O_3} + g_{Nd_2O_3} + g_{CeO_2} + g_{SO_3}\right. \\ &\left. + g_{MoO_3} + g_{CdO} + g_{PdO} + g_{NiO} + g_{SrO} + g_{ZrO_2}\right) \end{aligned} \qquad (4)$$

Equation (4)—**Difference based on correlation model** [50].

Where DC is the criterion for determining nepheline presence in samples made under CCC conditions, when DC ≥ 0.26, nepheline is predicted, while g_{oxide} is the mass fraction of the respective oxide.

It is of interest that when designing the model, the authors found that incorporating SiO_2 resulted in a decrease in accuracy, suggesting that the large effects and quantities of SiO_2 present in most glasses were masking the more subtle effects of the other oxides. The analysis performed showed that in the higher accuracy regions of PC space, ND and DC were the most important features, followed by Na_2O, Λ_{glass} and then CaO, while in the low accuracy regions, Na_2O was the most important feature, followed by DC, then ND, Λ_{glass}, and CaO in the stated order.

The low accuracy zone was found to exist where glasses with relatively similar compositions displayed different crystallization behaviors, and as a result, false negative and false positive results were located in close proximity to true positives and negatives. The authors of the DC model suggested reasons for the decrease in accuracy were either physics-based: glass compositions being sensitive to small changes in cooling rate, homogenization, composition, and other processing factors; or alternatively, data-based: not enough glass compositional data is available for a specific compositional space. The effects of these should not be downplayed, considering the effect of time (and thus rate) on nepheline crystallization [51, 52]. The impacts of the slightly different CCC rates used in these studies are not fully understood and may be especially important in the low accuracy region [50].

In subsequent research [53], multivariate analysis was performed by generating over 20 feature sets important in nepheline formation. This showed that one component varied at a time (OCAT) compositional studies, while useful, were essentially limiting the predictive power of the models, while bivariate effects were of increasing importance for the prediction of nepheline crystallization in HLW glasses. Feature sets were used in an attempt to discriminate between glasses with compositions that formed nepheline and those that did not. The feature sets were both structural (such as single bond strength or cation to anion radius ratio) and compositional (for example, the ratio or sum of certain oxides). The five strongest feature set interactions were found to be between: $\frac{X_{B_2O_3}}{X_{B_2O_3}+X_{Na_2O}}$ and $\frac{X_{SiO_2}}{X_{SiO_2}+X_{Al_2O_3}}$, $\frac{X_{B_2O_3}}{X_{B_2O_3}+X_{Na_2O}}$ and ND, $\frac{X_{B_2O_3}}{X_{B_2O_3}+X_{SiO_2}}$ and ND, $X_{Na_2O}+X_{Li_2O}+X_{K_2O}+X_{Cs_2O}+X_{Rb_2O}-X_{Al_2O_3}-X_{B_2O_3}$ and $\frac{X_{SiO_2}}{X_{SiO_2}+X_{Al_2O_3}}$, and finally $\frac{X_{B_2O_3}}{X_{B_2O_3}+X_{Al_2O_3}}$ interacting with X_{Na_2O} fraction (where Xi is the molar fraction of oxide i).

Regardless of the 20+ new feature sets, no combinations thereof could be used to completely separate glasses with compositions that did form nepheline and those which did not; and while they do give additional insight, they cannot make up for gaps or oversights in the data or methodology.

As moves are made to a more data-centric approach, it must be considered that not all data points were created equally. Certain data should carry more weight, while others may introduce unnecessary noise to the models (e.g., the DC model ignores SiO_2 as noted previously). This research simply shows an area where discrepancies may have been introduced into the data.

Ultimately, all models need to be linked to waste form chemical durability to be useful; and while models currently focus on nepheline prediction, the correlation between nepheline formation and residual glass composition, and resultant long term dissolution rates are even more likely to encounter complex nonlinear interactions [17, 46]. Thus, it is critical that research into the scientific mechanisms behind crystal formation and growth and the underlying mechanisms of dissolution continue, so that the outputs can feed back into the models.

A comprehensive list of potential sources of discrepancy is summarized below:

- **Choice of PCT vessel**—stainless steel and PFA TFE-fluorocarbon vessels are often used interchangeably, or the choice is not reported in the literature. When appropriately used, stainless steel vessels should be considered a "closed system" through which material transport is impossible. PFA TFE-fluorocarbon vessels should be considered "open systems" through which materials transport is possible, for example, O_2 or CO_2 [29]. Often these are chosen based on availability, and PCT results using different vessels are sometimes directly compared.
- **Compositional data voids**—Models, especially Machine learning (ML)/neural network (NN) models, require large amounts of data, and can benefit from datapoints being equally distributed throughout the compositional space, or more heavily present in lower accuracy portions of the compositional space, in regions where non-linearities take effect.
- **Insufficient data—**sufficient data does not exist to explain the complex non-linear relationships between oxides, groups of oxides, or substitution effects of pairs of oxides. Alternatively, major oxide components may be obscuring the more subtle effects of minor oxides.
- **Compositional correlation—**The presence of a compound or element in a waste stream often correlates with the presence of another. For example, the use of sodium hydroxide to dissolve aluminum cladding produced wastes enriched in Na and Al. Similarly, in the Bismuth Phosphate Process, where plutonium was co-precipitated with $BiPO_4$ while $Na_2Cr_2O_7$ was used as an oxidizer, this produced waste streams rich in Bi and P and containing Cr [6]. This results in single-component effects being harder to study, as they may not always be found isolated from certain counterparts in the waste.
- **Human error**—raw materials can be contaminated, and mismeasurements or recording errors can occur. Variance between multiple operators, practices, and instrumentation can exacerbate this. One key example of this is homogenization; often, if melts are not homogenized and re-melted, heavier elements may be disproportionated toward the bottom due to density-driven effects and hence may never make it out of the crucible into the sample that is measured. Conversely, melts kept at high temperatures for excessive times may result

in volatilization of lighter or more volatile elements. This effect is compounded if nominal compositions are reported.

- **Raw materials chemistry and purity**—not all laboratories use the same raw materials, and the quality/purity of raw materials or their method of storage may also vary between teams. It is well known that Al and Fe sources, for example, can have marked effects on a variety of nuclear waste glass parameters such as melt behavior, redox conditions, batch to melt conversion, and volatile oxide retention [54–57]. Furthermore, the redox ratio of multivalent species can affect the structure and properties of the underlying glass [58–60], and it has been shown that the amount of Fe and its redox state can affect the propensity of crystals to grow via either surface or bulk mechanisms [61]. It is also possible that other multivalent species may have similar effects. Additionally to control the behavior of certain aspects of the melt, such as the cold cap parameters [62], reducing agents are often used, which can in turn affect the oxidation state of the melt and potentially its propensity for nepheline formation, these effects have somewhat been studied [63], however, laboratory melts are often made without use of the same raw materials as full-scale melts. Moreover, the WTP melts will be conducted with minerals from a bulk commercial source, not lab-grade high-purity chemicals.
- **Use of nominal versus measured compositions**—and also the variance in the accuracy of the multiple methods and equipment used for measuring composition which is of particular importance for more volatile elements such as Cl or F, or for elements with a lower atomic number such as Li or B which may be difficult to detect accurately using certain techniques such as X-ray fluorescence spectrometry (XRF) or energy-dispersive X-ray analysis (EDX).
- **Different thermal histories of the glass**—it is possible that homogeneity was not fully achieved or that not all precursors to crystallization were fully removed due to slightly different thermal treatments before a CCC procedure was started. Known varied heat treatment schedules [48, 60] have been shown to affect crystallization [64]. Varied furnace accuracies and calibration methods may also have effects. For example, a 30 min hold time is often assumed to be sufficient to erase thermal history and reverse any crystallization that may have occurred during heating; this may require techniques such as high-temperature XRD (HTXRD) to confirm.
- **Different methods of crystal fraction determination—** The majority of the more recent publications that quantify crystal fraction do so by performing XRD on samples spiked with a known amount of an internal standard to calculate quantitative crystalline fraction (e.g., [20, 61, 65]), which has itself been carried out using multiple methods. When it comes to Rietveld refinement, both the standard and the amount added often vary between publications, as does the software used to perform the Rietveld analysis (e.g., GSAS/TOPAS/High Score Plus), with certain publications opting for a Rietveld-Reference intensity ratio (RIR) hybrid approach. However, apart from Rietveld refinement, simpler, semi-quantitative RIR approaches are also used, and semi-quantitative or visual/image processing methods are also sometimes applied. There are even differences in diffractometers, anode material, and even detectors, which may introduce some variation. Some studies have omitted the internal standard and simply analyzed peak intensities to extract semi-quantitative results [28, 48]. Scanning electron microscopy (SEM)/ EDX and Electron Probe Micro-Analysis (EPMA) [18] or even optical microscopy have also been used in conjunction with post-processing of image analysis data to estimate area and volume fractions [66, 67]. While all these methods may be considered viable options, their accuracies and resolutions are inconsistent.
- **Use of binary crystal quantification method**—within the database, certain glasses are categorized, and certain models work on the premise that 5% crystallization is equivalent to 99% by simply assigning a binary value to nepheline crystallization.
- **Furnace and thermocouple accuracy**—A wide variety of furnace designs, furnace controllers, and thermocouples, of differing makes and models, with varying accuracies, are available for purchase. Institutions will calibrate these at different intervals or sometimes not at all. Furnace chamber sizes and designs can affect the temperature profile inside the furnace, and elements and refractory linings age at differing rates with varying results. These can increase the uncertainty in the temperature profile, affecting reproducibility and introducing uncertainties into models created using the experimental data.
- **Melts extending beyond the bounds relevant to the project—**Modeling has been performed using melts that extend beyond the capabilities of the JHCM that will be used [37]. Glass melts at 1450°C, subsequently followed by modified CCC procedures starting at 1450°C are recorded in literature [35]. These are performed to fully melt the glasses in question; however, during cooling, these will allow for crystallization to occur within areas of the phase field, which will not be accessible during real canister melts.
- **Various crucible materials and states of crucible maintenance and cleanliness**—Irrespective of whether all the NP database glasses were made using platinum crucibles, not all platinum is equal, with pure Pt, 95% Pt 5% Au, 90% Pt 10% Rh, and zirconia grain stabilized (ZGS) platinum being commonly available in a laboratory setting. Furthermore, a brand-new crucible may perform differently when compared to a heavily used/worn one [68]. The surface interface, for example, may be altered; also, PtO_2 is a known nucleating agent [69] and if even small amounts of PtO_2 were to migrate into the CCC sample this may not always be detected if nominal compositions are reported, if compositional analysis is carried out before CCC heat treatment, or if the analysis method is insufficiently sensitive to detect low levels of such contaminants.

  Additionally, multiple methods of cleaning platinum are commonly employed; often, a low-durability glass is made with compositions using oxides such as B_2O_3, Na_2O, Li_2O, or K_2O, which are known to have an effect on the propensity for nepheline crystallization. The weak flux glasses are often washed away with HCl or HF baths, but if this is not performed to completion, or if any of the flux material makes its way into the subsequent sample, this could have a nontrivial effect on crystallization, especially since CCC samples are often relatively small.

- **Platinum melt versus Monofrax K3**—Another potential area for discrepancies between lab-scale melts and full canister melts is the use of platinum crucibles versus Monofrax K3-lined JHCM. Spinels are discussed in terms of being a key nucleating agent for other crystals [70, 71] to form, and although limited, Cr_2O_3 dissolves from the melter lining into the melt [37, 61, 72], something which is not observed with lab-scale platinum crucible melts.
- **Surface Area/Volume (SA/V) ratio effects**—This source of inaccuracy, identified and explored here in this context for (to the authors' knowledge) the first time, has received little to no consideration in literature, yet it could be one of the key factors as to why the waste loading predicted by almost all models is lower than can be achieved in real canister environments. In a real canister environment, the CCC cooling rate occurs along the canister centerline, by definition, away from the rapidly cooling steel walls. Therefore, no artificial nucleating surface can be present in this region of the canister, apart from any crystals or second phases that are also present (e.g., spinels, platinoid group metals, or intermetallics). Laboratory (crucible)-scale CCC experiments, however, have a proportionately large SA/V effect. This is introduced by preparing a relatively small glass sample, melted in direct contact with the crucible walls, something that is not present along the canister centerline. Furthermore, while in some internal laboratory standards, methods may exist for the production of CCC samples, in literature examples can be found showing that different SA/V ratios have been used for different samples, even, in some cases, in the same study [46]. The mode of nucleation versus surface [51, 61] can indeed be altered by composition, and hence this warrants further consideration.

The potential for sources of error introduced by SA/V effects is the focus of study of this research.

2 | Methods

In an effort to study SA/V effects, a new glass composition was designed to have the following properties:

- It should be balanced on the boundary of multiple models' abilities to predict whether it would or would not form the nepheline phase.
- It should be made up of the fewest oxides possible so that their interactions could be more readily studied and understood (without the excessive complexity that, for example, 15+ oxides may introduce), while still being relevant to the composition of the nuclear waste glasses being studied. The oxides chosen were the most plentiful in the wastes, combined with relevant GFC within sensible bounding limits.
- For the design of the KE1 composition, all the oxide wt. fr. values of each glass in the CCC database were averaged, and the 6 highest were arbitrarily used as a starting point for use in a simple optimization model, which would balance on the DC and SM models on the prediction boundary (after being normalized). The 6 components accounted for ~0.88 wt. fr. of all the CCC samples and where in order of weight: SiO_2, Al_2O_3, Na_2O, B_2O_3, Fe_2O_3, and Li_2O. CaO was present on similar levels to Li_2O; however, it does not feature in the DC model and was not required to balance on the knife-edge of the models. This does not mean it doesn't play a role in nepheline crystallization.

TABLE 2 | KE1 glass nominal composition in mol%, wt%, and as measured by XRF.

Oxide	Nominal mol%	Nominal wt%	XRF wt%
Al_2O_3	16.15	25.00	25.40 ± 0.11[a]
B_2O_3	19.11	20.20	19.94 ± 0.04[b]
Fe_2O_3	1.24	3.00	2.76 ± 0.15[a]
Li_2O	14.33	6.50	6.50 ± 0.00[c]
Na_2O	15.41	14.50	13.73 ± 0.32[a]
SiO_2	33.76	30.80	31.40 ± 0.25[a]
Total	100.00	100.00	

[a]Reported value measured using fused bead oxide program, error reported is statistical error on triplicate measurement of multiple fused beads across multiple batches.
[b]B_2O_3 value reported measured using cellulose pressed pellets oxide program, reported error is based on triplicate reading of a pressed pellet.
[c]Nominal Li_2O reported.

TABLE 3 | KE1 glass nominal in wt% broken down by element alongside composition as determined by EDX, based on the average of 20-point scans across 3 sites, error reported is standard error. *Nominal lithium value reported as it cannot be detected by EDX.

Element	Nominal wt%	EDX wt%
Al	13.23	12.07 ± 0.06
B	6.27	10.70 ± 0.22
Fe	2.10	2.13 ± 0.01
***Li**	3.02	3.02 ± 0.00
Na	10.76	9.22 ± 0.06
Si	14.40	12.55 ± 0.06
O	50.22	50.30 ± 0.07
Totals	100.00	100.00

With the above in mind, the composition dubbed "Knife Edge 1" (KE1) was designed with the following nominal and analyzed compositions shown in Tables 2 and 3.

The glass composition was generated by attempting to balance the SM P value at approximately zero while attempting to balance the DC value to approximately 0.26, which in both cases is the prediction boundary for nepheline formation. This was performed while ensuring that the compositional limits were within the region of high Al_2O_3 and Na_2O, consistent with HLW glasses, which was the case where the accuracy was lowest [50]. The Nepheline predictor values for KE1 glass can be seen in Table 4.

TABLE 4 | KE1 glass calculated nepheline predictor results, with red indicating that the model predicts nepheline will precipitate, while green suggests it will not, with yellow being used for Λ_{glass}, as the result is between the 0.55 and 0.57 boundary for more aggressive versus conservative prediction.

Nepheline predictor	Requirement for nepheline	Predicted outcome
ND	ND < 0.62	0.4381
OB	ND < 0.62 & Λ_{glass} > 0.55/.57	0.5659
P (SM opt.)	$p < 0$	−0.0111
P (SM con.)	$p < 0$	−0.0302
DC	DC ≥ 0.26	0.2580

Note: For both DC and SM models (as well as Λ_{glass}), the result is exceedingly close to the boundary, and as confirmed by the figure, this composition is therefore in the low accuracy area for prediction.

Multiple glass batches were prepared and used over the course of this study, ranging from 100 to 400 g of glass each time. The typical melt parameters were as follows: the glasses were batched with laboratory-grade (> 99.5% purity) SiO_2, Na_2CO_3, $Al(OH_3)$, H_3BO_3, Fe_2O_3, Li_2CO_3, and mixed for 3.5 min in a Willy A. Bachofen AG (WAB-GROUP) Type T2 C TURBULA mixer. A portion of the mixed batches was then gradually loaded into a ZGS Pt crucible, which was placed in an electric furnace at 1150°C, and batch decomposition was allowed to occur before loading more batches over the course of 1 h, until all the batches were added. An initial pour was conducted onto a cast-iron plate. The resultant glass was crushed in a WC vibratory mill before being re-melted, again at 1150°C, to homogenize for another hour. These were then consolidated into glass bricks by being poured into a cast iron plate and annealed at 415°C for 1 h and being allowed to gradually cool to room temperature. The annealing temperature was selected to be ~20°C below T_g identified at 10°C/min. These bricks were then sectioned using a diamond saw blade and a WC vibratory mill as required for individual experiments.

2.1 | Characterization of KE1 Glass

Thermal characterization was performed on the glass by placing and tamping 20 ± 0.5 mg of glass powder in an alumina pan. A variety of heating rates (1°C, 2°C, 5°C, 10°C, 15°C, 20°C, 25°C, 30°C/min) were applied in the range 30°C–1000°C using a TA Waters SDT650 DSC, and both DSC and TGA data were recorded.

The instruments accompanying software (TA Trios) was used to extract T_g values from the DSC data. At 10°C/min, T_{go} onset was found to be T_{go} = 431.72°C ± 0.06°C[1] and T_g midpoint was found to be T_g = 437.60°C ± 0.13°C[1].

The DSC data also allowed for the determination of the first exothermic crystallization peak (although two clear exothermic peaks existed between T_g and T_{melt}). When measured at 10°C/min, crystallization onset was determined to be T_x = 548.54°C ± 0.06°C[1] while peak crystallization temperature was determined to be T_p = 582.55°C ± 0.34°C[1]. The normalized enthalpy was determined by measuring the area under the peak, by first identifying the minima and maxima on the first-order differential (smoothed) containing the inflection points underneath the peak; these were provided to the Trios software as the start and endpoint of the crystallization exotherm. The entropy was determined to be ΔH = 102.68 ± 0.61 J/g[1], the peak width half height was FWHM = 46.84°C ± 0.06°C[1], with the peak height being measured at H_p = 0.347 ± 0.003 W/g[1].

Multiple heating rate data allowed for the use of the empirical logarithmic heating rate extrapolation method [73], and the thermal events were estimated at 0.1°C/min heating rates to approximate near equilibrium conditions. The extrapolated glass transition temperature was found to be T_g = 400.1°C, and the extrapolated crystallization peak was found to be T_p = 430.4°C.

Using the Kissinger method [74], the activation energy (E_a) can be estimated to be 152.5 kJ/mol. Due to the vast compositional range of HLW sodium borosilicate (NBS) glasses, the E_a value deduced from exothermic crystallization peaks can vary by at least an order of magnitude, with typical ranges being 50–500 kJ/mol or greater. However, lower activation energies tend to correlate with ease of crystallization [61, 75–77], and thus, it is entirely possible that the E_a value for sample KE1 may be on the borderline for crystallization under CCC conditions.

An isostatic crystal growth experiment was performed at 488°C on the KE1 glass sample. Approximately 0.5 g was placed in multiple alumina pans. The calibrated oven was allowed to stabilize for 5 h, and then the pans were quickly placed in the oven and individual pans were removed after 1, 5, 15, 30, and 60 min, and then in increments of 1 h up to 6 h hold times. Additionally, one pan was kept in for 24 h. Using the Avrami method [78–80], the Avrami exponent n was determined to be n = 1.51 ± 0.25, suggesting that, for this glass composition, crystal growth is a 1D or 2D controlled process. However, it should be noted that only the 24, 6, 5, 4, 3 h samples yielded usable crystal fraction results, and at 6 h $X_{Nepheline} < 4$ wt% and $X_{Eucryptite} < 2$ wt%, and a more thorough investigation should be conducted. The determining factor for the difference between canister performance and lab scale performance for these compositions in the low accuracy region, may be the combination of relatively low activation energy and 2D versus 3D growth [61], especially as crystal growth of this nature (powdered, in contact with a crucible wall) is not representative of real world canister melts, however, this is suggested as future research. The Avrami constant deduced here is not unlike similar samples in literature. McClane et al. [51] derived similar values in nepheline-bearing samples, which showed surface nucleation (values between n = 1.28 and 2.05), again showing that composition can drive the mode of nucleation.

A ~25 mm long × Ø ~5 mm cylindrical rod was prepared and a Netzsch DIL 402 Expedis dilatometer was used with a heating rate of 10°C/min to measure the thermal expansion of KE1 glass; $\alpha = 11.74 \times 10^{-6}$ /K was determined between 50°C and 300°C, furthermore the dilatometric softening point, T_d, under these conditions was determined to be T_d = 462°C using the Netzsch Proteus software.

Approximately 10 g of glass shards were placed into a ~10 cm rectangular alumina boat, which was subsequently loaded into an

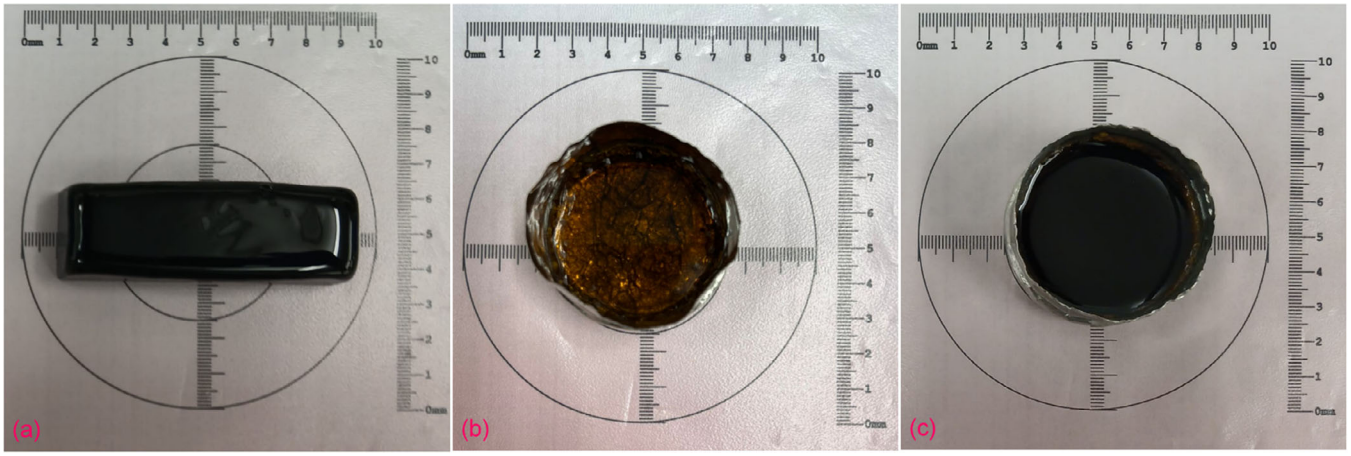

FIGURE 5 | (a)–(c) Three samples of KE1. (a) KE1_glass, melted at 1150°C and annealed at 415°C, confirmed to be X-ray amorphous by XRD. (b) KE1_CCC_20 after CCC heat treatment, still in the Pt Au crucible. (c) KE1_CCC_66 after CCC heat treatment is still in the Pt Au crucible.

Elite gradient tube furnace. The furnace was ramped to ~1200°C for 30 min to fully melt the sample. The temperature gradient across the sample was then measured to be ~885°C–640°C using an R-type thermocouple. Experiments were initially conducted for 3 days and then 7 days, but no discernible crystals could be seen by optical microscopy. The experiment was repeated for 14 days, and the last crystal grown was determined by optical microscopy and fitted against the measured temperature profile. The liquidus temperature using this method was found to be T_{Liq} = 800°C ± 10°C. In this instance, the error was determined by previous measurements on glasses with a known liquidus using a similar approach.

To prepare XRF samples, ~1 g of powdered sample was mixed with ~10 g of lithium tetraborate flux containing 0.5wt% lithium iodide $(Li_2B_4O_7)_{0.995}(LiI)_{0.005}$. This mixture was loaded into a 95% Pt 5% Au crucible using a Claisse Leo Neo Fusion Instrument. The mixture was heated up to 1065°C, and the molten mixture was poured into a 95% Pt 5% Au casting mould. This cooled to form a homogenous "fused bead" glass disc. The fused beads were analyzed in a Rigaku ZSX Primus IV wavelength dispersive X-ray fluorescence spectrometer, the results compared to an internally calibrated oxide standards [81].

Finally, Archimedes' bulk density measurement in water was performed on multiple glass shards in triplicate, and the glass was found to have a density of $\rho = 2.4654 \pm 0.0031$ g/cm^3, with the stated error being the standard error on three measurements.

2.2 | Sample Preparation

A multi-faceted experimental approach was designed to test the following hypotheses:

- The fraction of crystalline components reported is affected by SA/V.
- Increasing the SA/V ratio during the application of a CCC thermal profile increases the measured crystal fraction measured post treatment in some glasses.
- SA/V of CCC sample affects final PCT-B chemical durability results.

A Nabertherm P470 furnace with a B400 controller was used for all CCC heat treatments. To accurately calibrate the furnace, a calibrated Pt-Rh type R thermocouple was used to compare the furnace set temperature to that measured by the thermocouple. Starting at 200°C, the temperature was measured for 5 h in increments of 100°C up to 1200°C, and the average of the last hour of each hold was used to fit a second-order polynomial to convert furnace set temperature to the actual temperature being achieved. The same thermocouple was used during all CCC procedures, and an average deviation of ~5°C was achieved from the expected CCC procedure.

For this study, two portions of the KE1 glass sample (determined to be vitreous by XRD, as shown in Figure 10) were sectioned and placed in two separate identical 95% Pt 5% Au crucibles with a diameter of 5 cm and a wall height of 2.5 cm. A Pt lid was placed over the crucibles, and they were heat-treated according to the CCC profile. The only difference between the samples was that one contained 20 g of KE1 and the other 66 g. Thus, they were named KE1_CCC_20 and KE1_CCC_66, respectively. The 20 g sample, therefore, had a larger SA/V ratio (Figure 5).

Finally, ~10 g of sample KE1_glass was placed in a Pt crucible and heated to 579°C (near the first crystallization exotherm) for 96 h. This temperature allowed for both nucleation and crystal growth to occur and thus would allow for the absolute worst-case scenario for nepheline growth. This sample was named KE1_579C_4day (Figure 6).

A subset of the samples was prepared for PCT-B as per ASTM C1285-21 [29]. They were powdered in a WC mill and sieved to separate particle sizes of between 75 and 150 μm by using US Standard mesh sizes −100 to +200. The particles were cleared of adhering fines by repeatedly washing first in DI water and then in non-polar solvents of decreasing densities. The mixtures were gently agitated, and the particles were allowed to settle before the surface liquid was removed by syringe. This was repeated until the samples were satisfactorily clear of fines as verified by optical

TABLE 5 | Summary of all the samples used in this study.

Sample name	Preparation	Crystallinity
KE1_Glass	Melted, crushed, and re-melted in a Pt Rh crucible at 1150°C for 1 h, poured, and annealed at 415°C	Vitreous (see Figure 10)
KE1_CCC_20	20 g of KE1_Glass, placed in a Pt Au crucible, with a Pt lid, re-melted at 1150°C for 30 min before a CCC cooling profile being applied.	Partially crystalline (see Figure 11)
KE1_CCC_66	66 g of KE1_Glass, placed in a Pt Au crucible, with a Pt lid, re-melted at 1150°C for 30 min before a CCC cooling profile being applied.	Partially crystalline
KE1_579_4day	~10 g of KE1 glass placed in a Pt crucible, heated to 579°C, and held there for 4 days	Visually phase separated, crystal growth confirmed by SEM (see Figures 6i and 13a,b)
DWPF EA	DWPF EA [30] glass provided by PNNL.	As received.

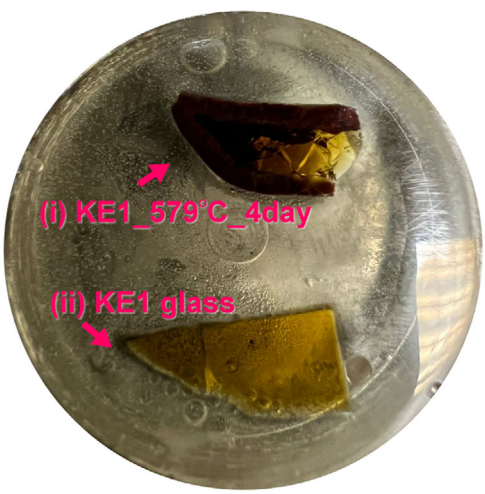

FIGURE 6 | Two different KE1 samples encased in epoxy resin, polished, and ready for SEM. Sample (i) is a small amount of KE1 glass that has been heat-treated inside a platinum crucible for 96 h at 579°C, approximately at the peak crystallisation temperature. Sample (i) is referred to as KE1_579C_4day in this document. Sample (ii) is a small shard of KE1_glass broken off from the bar shown in Figure 5a.

microscopy. The powders were then dried at 110°C before being stored in a vacuum desiccator until all samples were prepared and ready for PCT.

Alongside the KE1 variants (KE1_glass, KE1_CCC_20, and KE1_CCC_66) a sample of DWPF EA glass [30] provided by PNNL was also prepared for PCT analysis;

The samples are summarized in Table 5.

2.3 | Experimental Approach

Optical micrographs of the KE1_CCC_20 sample were taken to compare the surface in contact with the Pt crucible and the surface in contact with air before they were sectioned and powdered for further XRD and PCT-B experiments. Scanning electron microscopy (SEM) images were also taken of the sample in contact with the platinum, to determine the size of the nanocrystals. The surface was leveled, and carbon sputtered, but no other preparation was undertaken, as grinding and polishing would have taken away the surface of interest.

SEM and energy dispersive X-ray spectrometry (EDX) were performed on the KE1_579C_4day sample. The sample was prepared by encasing it in epoxy resin so that its cross-section was exposed, then grinding and polishing were performed using a Buehler AutoMet 250 with: SiC 600 grit (water-cooled), SiC 800 grit (water-cooled), 3 μm diamond suspension with a TexMet cloth pad, and finally a mix of 1 μm alumina and silicon suspension with a MasterTex cloth pad.

All SEM was conducted with a FEI Quanta 650 microscope, and EDX was performed with an Oxford Instruments X-Max detector. Scans were conducted using a spot size of 4.5, an acceleration of 20 kV, and a WD~10 mm. Compositions were determined by taking 20-point scans for 20 s across 3 or 4 sites and averaging the counts across similar regions. An Emitech K950X carbon sputter coater was used to prepare the samples.

A Malvern Panalytical Empyrean powder X-ray diffractometer with a Cobalt X-ray tube (K_α = 1.7902 Å) and a PIXCEL-3D area detector was used to characterize the degree to which any sample was amorphous or crystalline [82].

Both monolithic samples and powdered samples were run on a spinner stage for improved counting averages, and all samples were measured from 10–110° 2ϑ, with a step size of 0.013° 2ϑ and time per step of 223.125 s. The scans were performed with an automatic divergence slit (ADS), but plots reported here have undergone ADS to fixed divergence slit (FDS) software conversion. Either 1° or 2° slits were used, and a 20-mm irradiated sample length and mask size were used for powdered samples, while due to the smaller dimensions after cracking, a 5-mm irradiated length and a 5-mm mask were used for the monoliths.

Where Rietveld refinement was performed ~100 mg of powdered sample was mixed with ~1–2 mg of Silicon standard NIST 640 g [83] in an agate pestle and mortar, and spread onto a

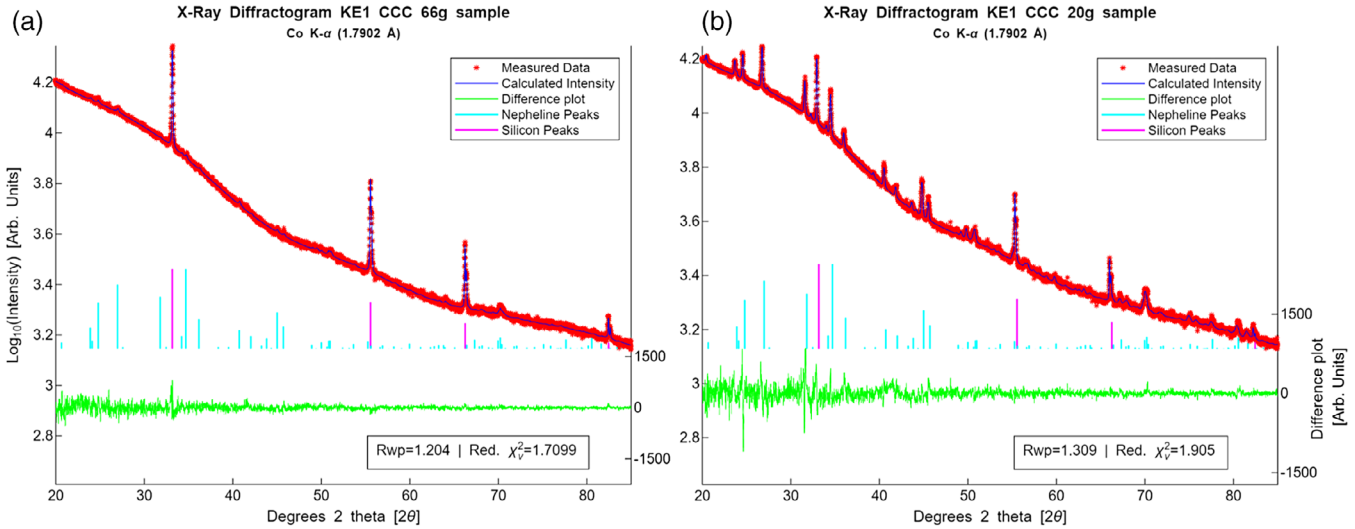

FIGURE 7 | (a) and (b) KE1 CCC XRD Rietveld refinement difference plot. (a) Left: KE1_CCC_66 g sample (low SA/V) average of entire sample. Diffraction pattern dominated by Silicon Standard Peaks. (b) Right: KE1_CCC_20 g sample (high SA/V) average of entire powdered sample. Considerably more diffraction peaks are present, which correspond to Nepheline.

monocrystalline silicon wafer using isopropanol. The sample was allowed to dry before being analyzed.

Using the Malvern Panalytical High Score Plus software, initial Automatic Rietveld refinement was performed using the crystallographic information files (CIF) discussed in Section 3.2 X-ray diffraction, before proceeding with a manual parameter optimization, starting with a Chebishev I 15 parameter background fit (due to the highly amorphous and low crystallinity nature of the samples), followed by the profile function parameters, unit cell parameters and then the atomic coordinates, temperature factors and finally the occupancy, with these parameters being refined first for the well-defined silicon (Figure 7).

PCT-B chemical durability testing was performed in Teflon bottles that were either cleared and checked for fluoride as prescribed by ASTM C1285-21 or had already been used sufficiently and cleared the fluoride check threshold as stipulated in the standard. As well as triplicate blanks, ~1 g of each sample was prepared in triplicate and put in ~10 mL of type 1 DI water with a calibrated pipette, and the weight was recorded, so that the following conditions stipulated by the ASTM standard were met, such that $\frac{V_{solution}}{m_{solid}} = 10 \pm 0.1 \frac{cm^3}{g}$.

The 7 day ±2% PCT-B tests were conducted at 90°C ± 2°C using Type 1 DI water with confirmed 18.2 MΩ resistance. Once the tests were complete, an aliquot of each sample was taken, and the pH was measured and recorded. Then, using a syringe with a 45 μm filter tip, samples were collected for ICP, with multiple dilutions being prepared for ICP testing.

Mixed element standards were prepared for ICP by diluting from 1000 ppm Perkin Elmer single element standards of Al, B, Ca, Li, Na, and Si. All samples and standards were prepared in 1% HNO_3 solution, and all had a 1 ppm Indium standard diluted from a 1000 ppm Perkin Elmer single element standard, with the In to be used as an internal calibration standard. 11 standard solutions were prepared between 0 and 100 ppm in increments of 10 ppm.

ICP-OES was performed using an Agilent 5900 ICP-OES, with each dilution and each PCT triplicate being measured in replicate 5 times so that an average value and a standard error could be calculated.

Finally, a TA Waters SDT650 DSC was used to perform DSC analysis on 4 samples of KE1 glass, all weighing 20 ± 0.5 mg, taken from the original block of glass (Figure 5a). These were loaded into alumina crucibles, with the only difference being their particle size. One 20 mg cubic monolith was prepared by sectioning and gently polishing until it was of the desired weight, one sample was simply powdered in a WC mill, and finally the remnant powders from the PCT preparation, one with size fraction less than 75 μm (too small for PCT-B testing) and one with size fraction greater than 150 μm (too large for PCT-B testing) made up the last two samples. This was carried out to create compositionally identical samples examined in identical conditions, with the only variable being the SA/V ratio. The samples are summarized below:

- **DSC sample 1**: 20 mg monolith of KE1 glass prepared by sectioning, grinding, and polishing. This sample had the lowest surface area to volume ratio of the DSC samples.
- **DSC sample 2**: 20 mg of KE1 glass powdered and sieved to only contain particles with a size fraction greater than 150 μm. This sample had the second-lowest surface-to-area volume of the DSC samples.
- **DSC sample 3**: 20 mg of KE1 glass powder, not sieved, therefore containing an amalgamation of powders greater than 150 μm, below 75 μm, and particle size in between. This sample had the second-highest surface-to-area volume of the DSC samples.

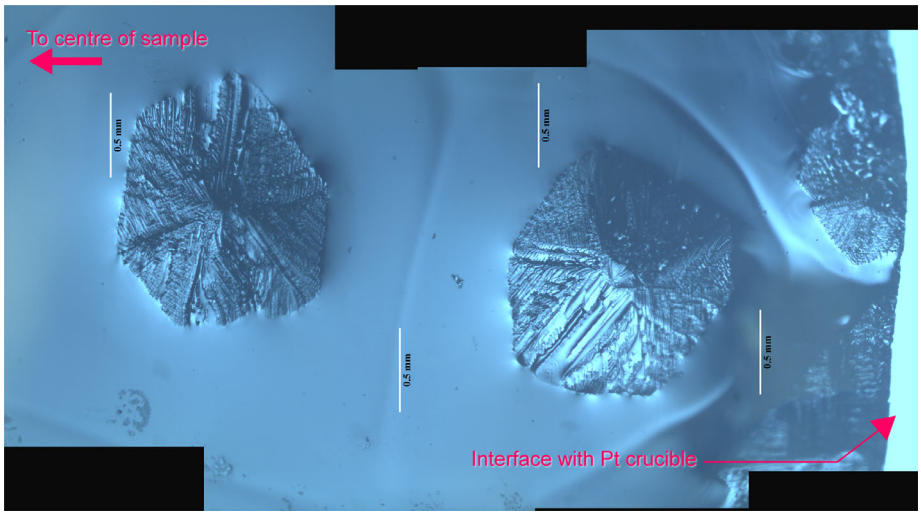

FIGURE 8 | Composite image of multiple micrographs of the top surface of the KE1_CCC_20 sample. The right-most area shows where the sample would have been in contact with the platinum crucible during heat treatment, while the center of the sample will be to the left of this image.

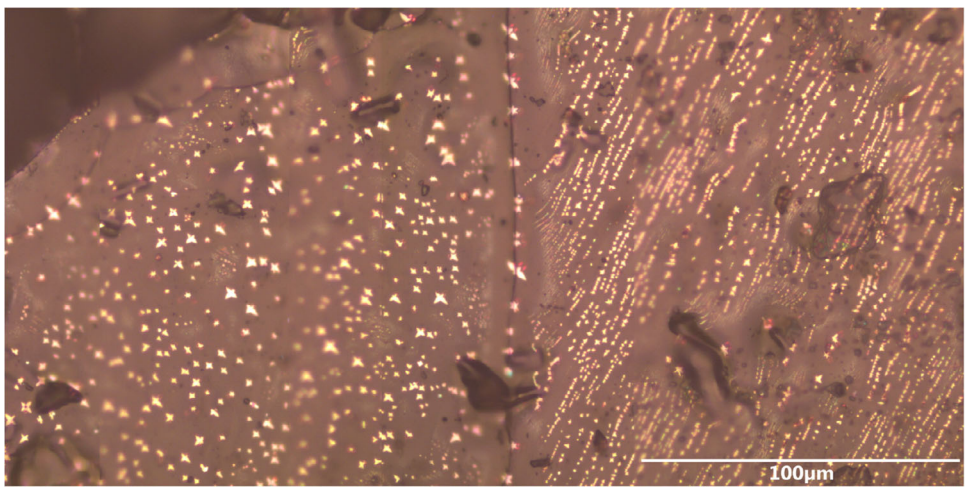

FIGURE 9 | Composite image of multiple micrographs of the bottom surface of the KE1_CCC_20 sample. The top left of the image shows the circular outline of the sample that would have been in contact with the Pt crucible during CCC heat treatment. Multiple orders of magnitude more crystals can be seen that are much smaller.

- **DSC sample 4**: 20 mg of KE1 glass powdered and sieved to only contain particles with a size fraction less than 75 µm (the fines). This sample had the largest surface area to volume ratio of the DSC samples.

A heating rate of 10°C/min was run on these samples, and DSC/TGA data were recorded.

3 | Results

3.1 | Optical Microscopy

Figures 8 and 9 show optical micrographs from both the top (in contact with air) and bottom (in contact with the Pt crucible); visual inspection alone shows that highly different crystallization phenomena have occurred.

Inspecting the top surface of the sample, around the internal circumference of the platinum crucible where the crucible contacted the sample, the crystals formed continuously around the sample. Certain ~1 cm long nepheline crystals grew 2–3 cm toward the center of the sample; however, the center of the sample was visually crystal-free.

As the Pt-Au (5 wt% Au) crucible has very thin walls and is malleable, it was possible to manipulate and remove the samples after heat treatment, with only minor sample damage (no sample stuck to the crucible). An optical micrograph of the bottom of the sample revealed a large number of micro and potentially sub-micron "X"-shaped projections.

SEM microscopy of the same surface revealed countless nanocrystals of the same morphology. This suggests that while nucleation is possible at the glass-air interfacial boundary, it is

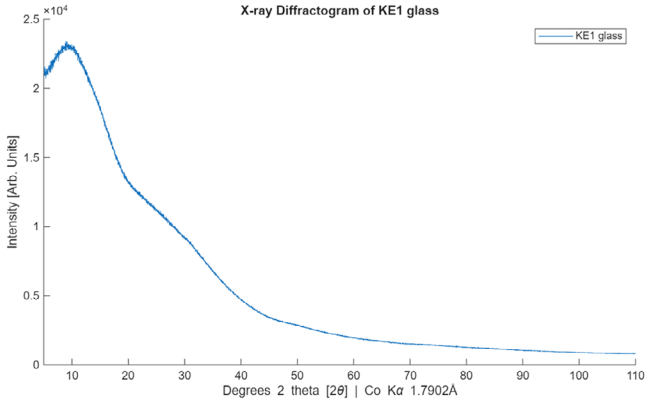

FIGURE 10 | XRD pattern for KE1 glass run as a powdered sample with a 1° slit width and 20 mm mask ADS to FDS correction applied.

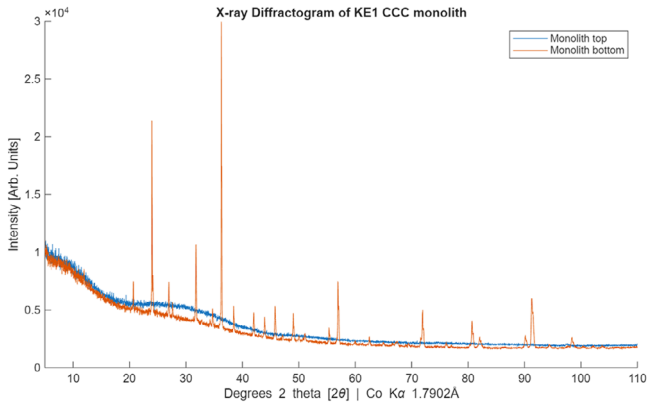

FIGURE 11 | Two overlaid XRD patterns derived by scanning the same monolith of KE1_CCC_20 g, the diffuse scattering showing that the center of the sample exposed to the air did not crystallize (blue), while the center of the bottom face in contact with the Pt crucible crystallized substantially (orange). Scan parameters were identical for both scans. Scans performed using a 5-mm mask, 2° slit ADS to FDS correction applied.

many orders of magnitude less likely than at the glass-crucible boundary. At the glass-air interface, when a crystal nucleates during the many hours of CCC cooling, it has potentially hours to grow, meeting no obstructions to its growth, allowing it to reach dimensions on the centimeter scale. Conversely, at the platinum interface, when the thermodynamics and kinetics allow countless crystals to nucleate, their growth is rapidly limited by the neighboring crystals, and hence they do not reach comparable sizes to those on the top of the sample. SEM analysis showed that the crystals at the platinum interface were on the sub-micron scale.

3.2 | X-Ray Diffraction

Powder X-ray diffraction measurements were performed on the glass post-annealing. This confirmed the sample was X-ray amorphous and no detectable crystals were present, as shown in Figure 10.

The side edges in contact with the Pt of the KE1_CCC_20 sample (shown in Figure 5b) were sectioned so that the center of the sample (with ~5 mm^2 surface area) could be placed into a spinner sample holder, initially with the air interface in the path of the X-rays and subsequently inverted with the platinum contact interface placed in the path of the X-rays. The center of the monolith at the glass-air interface showed only minor peaks at 10° 2ϑ; however, the bulk of the diffraction pattern can be described as a typical amorphous "hump" or diffuse scattering. This cannot be said with regard to the bottom side of the sample, which was demonstrably more crystalline. Both diffraction patterns are overlaid in Figure 11.

Using the "search and match" function the on the Malvern Panalytical High Score Plus software, integrated with the ICDD PDF-5+ database [84], the phases identified on the platinum contact interface by scanning the surface of the monolith were ICDD:04-016-1739 Nepheline, syn ($Na_{3.205}Al_{3.205}Si_{4.795}O_{16}$) hexagonal space group number 173 $P6_3$ [85] and ICDD:04-016-6555 Trinepheline, syn ($Na_{0.98}Al_{0.98}Si_{1.02}O_4$) monoclinic space group number 4 $P2_1$ [86]. The layer containing these phases is seemingly very thin as once the samples were powdered (in preparation for PCT) and these were re-scanned and Rietveld analysis was performed (averaging the crystal fraction across the entire monolith) the sharp Bragg peaks superimposed over the diffuse scattering (amorphous) background are more readily assigned to ICDD:04-016-1737 Nepheline, syn $Na_4Al_4(SiO_4)_4$ hexagonal space group number 173 $P6_3$ [85]. This suggests that a more silicon-rich form of nepheline nucleated at the glass-platinum interface, with a stochiometric (Na:Al:Si balanced) variant nucleating further into the sample, beneath the surface.

Of further note when a compositionally-identical sample of KE1 underwent isothermal heat treatment at 488°C in an effort to determine the Avrami constant, and was not cooled from molten per the CCC procedure, not only was ICDD:04-016-1737 Nepheline, syn $Na_4Al_4(SiO_4)_4$ hexagonal space group number 173 $P6_3$ identified, but alongside it a Lithium Aluminosilicate Phase was also identified, namely: 04-023-0527 Eucryptite $LiAl(SiO_4)$ Orthorhombic space group number 29 $Pca2_1$ [87]. Eucryptite, much like nepheline, has been found to reduce the chemical durability of nuclear waste glasses [88]. From studying its chemical formula, it is possible to speculate as to why, since the formation of this phase would remove more network formers (Al/Si) from the glass than modifiers (Li in this instance), similarly to nepheline. Phases and polymorphs very similar to those listed above have regularly been found in high alumina high sodium nuclear waste glasses [20].

The samples were powdered for PCT-B and XRD analyses, and are described here. These are more representative of what would occur during a CCC/PCT sample (not just monolith surface examination). A sample of KE1_glass (amorphous bulk glass), KE1_CCC_20 (high SA/V CCC sample), KE1_CCC_66 (low SA/V CCC sample), and the isothermally heat-treated KE1 glass were powdered for XRD. Rietveld refinement was performed as necessary to determine the crystalline fraction. With the exception of the isothermally treated glass, all these powders were subsequently processed for PCT-B analysis.

TABLE 6 | Summary of crystal fraction by portion of CCC sample analyzed.

Sample	Subsection	wt%
KE1_CCC_20	**Edge**	7.0 ± 0.7
KE1_CCC_20	**Centre**	2.4 ± 0.3
KE1_CCC_20	**Monolith average**	3.0 ± 0.1
KE1_CCC_66	**Monolith average**	0.8 ± 0.1

The KE1_CCC_20 sample was sectioned, and Rietveld refinement was performed in order to determine the crystallinity of the different sub-sections. The first section contained mostly sample edge, close to the Pt wall, the next section was from the center of the monolith, some samples in contact with the bottom surface will have been included, but no edge. Finally, the entire sample was also powdered and homogenized, to represent the average of the entire sample.

The KE1_CCC_20 sample was found to contain a higher crystalline fraction closer to the Pt-glass interface (7.0 ± 0.7 wt% crystalline and 93.0 ± 0.4 wt% amorphous), while the center of the sample was found to have (2.4 ± 0.3 wt% crystalline and 97.6 ± 0.2 wt% amorphous), the average of the entire monolith was found to be in between the two sectioned samples (3.0 ± 0.1 wt% crystalline and 97.0 ± 0.1 wt% amorphous); conversely the KE1_CCC_66 sample was found to be almost entirely amorphous (0.8 ± 0.1 wt% crystalline and 99.2 ± 0.1 wt% amorphous), however, it must be recognized that error quantification becomes difficult as there are almost no peaks for the refinement to latch on to. Results of crystal fraction determination summarised in Table 6.

However, the refinements yielded an Rwp = 1.309 for the KE1_CCC_20 sample and Rwp = 1.204 for the KE1_CCC_66 sample (see Figure 7a,b). Where Rwp (Weighted-profile R factor) measures the "goodness of fit" by comparing the weighted squared differences between calculated and observed intensities, divided by the weighted variance of the observed data, Rietveld refinement attempts to minimize this by varying a multitude of fit parameters representative of the instrument used and the crystallographic sample being studied [89].

The above Rietveld refinement shows that sample preparation, methodology, and sectioning, yields result which in this case, varied by more than 2× in terms of crystal fraction, the PCT-B results will show that this will have a considerable effect on chemical durability.

3.3 | Product Consistency Tests

Product consistency test B (PCT-B) [29] using ICP-OES to measure elemental release was then performed. To confirm that the results could be relied upon, a standard glass was measured alongside the samples of interest. DWPF EA glass is the standard glass for PCT-B analyses, and accepted waste forms must outperform EA glass in terms of Si, Na, and B release during a concurrent 7-day PCT-B test. EA glass is comprised of over 10 common nuclear waste glass component oxides (as listed in Table 7), whose properties have been well documented, especially with regard to its chemical durability.

TABLE 7 | DWPF EA target glass composition [30].

Oxide	Target glass composition wt%
Al_2O_3	3.67 ± 0.18
B_2O_3	11.12 ± 0.56
CaO	1.13 ± 0.06
Fe_2O_3	8.08
FeO	0.89
K_2O	0.04 ± 0.00
La_2O_3	0.41 ± 0.04
Li_2O	4.28 ± 0.21
MgO	1.66 ± 0.08
MnO	1.34 ± 0.07
Na_2O	16.71 ± 0.84
NiO	0.61 ± 0.06
SiO_2	48.95 ± 0.90
TiO_2	0.71 ± 0.07
ZrO_2	0.41 ± 0.04
Total	100.01

The PCT-B test results for DWPF EA glass supplied by PNNL obtained in this study are broadly comparable to major multi-operator, multiple repeat test characterizations performed in the past [30]. A comparative summary can be seen in Table 8.

The pH value obtained by the characterization study prepared at the Savannah River Site for the US Department of Energy [30] study was 11.85 with a standard deviation of 0.1, while the pH upon unloading measured in this study was 12.07 with a standard deviation of 0.02 and a standard error of ±0.01.

The full PCT-B results for all elements analyzed in this study are shown in Tables 9 and 10.

As expected, the KE1_glass sample outperformed the CCC samples in terms of normalized concentration (normalized by the weight fraction of the element present in the entire waste form or NCi) for Al, B, Li, and Na. The inverse is true with regard to Si release; this is most likely due to silica being incorporated into highly durable nepheline crystals. Regardless, the Si release was considerably lower than that released by DWPF EA glass for all samples. No normalized release for calcium was measured for any of the KE1 samples, as no measurable levels of Ca were present in the sample. For all other elements, Al, B, Li, and Na, the best performing sample was the KE1_glass, followed by the KE1_CCC_66, the low SA/V sample, while the worst performing was the high SA/V sample KE1_CCC_20.

Table 11 shows the relative increases and decreases in normalized concentration release (NCi) for each leached element compared to KE1_glass. While modest increases of between 1.32 and 1.44

TABLE 8 | DWPF EA measured elemental release in ppm and normalized concentration NCi for B, Li, Na, and Si obtained by SRS [30] and in this study, for direct comparison.

Leachate concentration	Mean (ppm) (Jantzen) [30]	Mean (ppm) (this study)	Mean (g/L) (Jantzen) [30]	Mean (g/L) (this study)
B	587 (43)	626 (8.6)	16.695 (1.222)	18.122 (0.269)
Li	190 (14.5)	195 (3.2)	9.565 (0.735)	9.798 (0.200)
Na	1662 (112)	1350 (9.1)	13.346 (0.902)	10.894 (0.090)
Si	893 (86)	957 (16.3)	3.922 (0.376)	4.185 (0.087)

Note: Values in brackets represent the standard deviation.

TABLE 9 | Elemental release was measured for Al, B, Ca, Li, Na, and Si for all samples in this study, with standard error reported.

ppm	KE1CCC skinny	KE1	KE1 CCC V3 bulk	DWPF EA
Al	92.95 ± 4.227	63.739 ± 1.228	64.162 ± 0.206	3.237 ± 1.167
B	914.025 ± 17.924	286.407 ± 6.971	411.029 ± 12.739	625.862 ± 4.373
Ca	0.28 ± 0.219	0.01 ± 0.003	0.007 ± 0	0.33 ± 0.067
Li	345.908 ± 6.128	104.155 ± 2.909	148.651 ± 4.982	194.832 ± 1.871
Na	686.074 ± 1.835	237.695 ± 6.763	313.655 ± 11.287	1350.461 ± 5.268
Si	21.828 ± 1.474	60.812 ± 0.86	44.034 ± 0.324	957.491 ± 9.392

TABLE 10 | Normalized concentration released NCi values for Al, B, Ca, Li, Na, and Si for all samples in this study, with standard error reported.

NCi (g/L)	KE1_glass	KE1_CCC_20	KE1_CCC_66	DWPF EA
Al	0.482 ± 0.011	0.702 ± 0.0390	0.485 ± 0.002	0.167 ± 0.074
B	4.565 ± 0.136	14.569 ± 0.350	6.552 ± 0.249	18.122 ± 0.155
Ca	0.000 ± 0.000	0.000 ± 0.000	0.000 ± 0.000	0.041 ± 0.010
Li	3.449 ± 0.118	11.455 ± 0.249	4.923 ± 0.202	9.798 ± 0.115
Na	2.210 ± 0.077	6.378 ± 0.021	2.916 ± 0.129	10.894 ± 0.052
Si	0.422 ± 0.007	0.152 ± 0.013	0.306 ± 0.003	4.185 ± 0.050

TABLE 11 | Normalized concentration released NCi (g/L) values of a given element for different samples, normalized and compared against KE1_glass as a baseline to show relative increase or decrease.

NCi (g/L) vs. KE1_glass	KE1 CCC (20 g)	KE1 CCC (66 g)	DWPF EA
Al	1.46x	1.01x	0.35x
B	3.19x	1.44x	3.97x
Ca	NA	NA	NA
Li	3.32x	1.43x	2.84x
Na	2.89x	1.32x	4.93x
Si	0.36x	0.73x	9.92x

Note: Values greater than 1 indicate higher leaching compared to KE1_glass by the factor stated, while values less than 1 indicate a leaching rate lower than KE1_glass.

times occur for B, Li, and Na for the KE1_CCC_66 sample when compared to KE1_glass, the performance for KE1_CCC_20 for the same elements ranges between 2.89 and 3.32 times the normalized concentration released. With the exception of Si, all the elements in the samples (Al, B, Ca, Li, and Na) were more readily leached from the high SA/V sample, while being more readily retained in the low SA/V sample. Of note, the low SA/V sample (KE1_CCC_66) does not fail any comparison with respect to DWPF EA glass, while the high SA/V sample (KE1_CCC_20) fails with regard to Li release and comes relatively close with regard to B release. This can be very clearly seen in Figure 12b,d. Table 12 shows the same relative increase and decrease in normalised concentration release in the KE1 samples compared to DWPF EA glass.

This glass would fail the required test for full vitrification based on comparison with DWPF EA glass as outlined in the WAPS [31] if made and tested with a high SA/V of sample to crucible contact area, yet it would pass if the same composition was made with a low SA/V; something which is not accounted for by the requirements of the test. This suggests that methodology is a key determining factor in the go/no-go decision for a nuclear waste

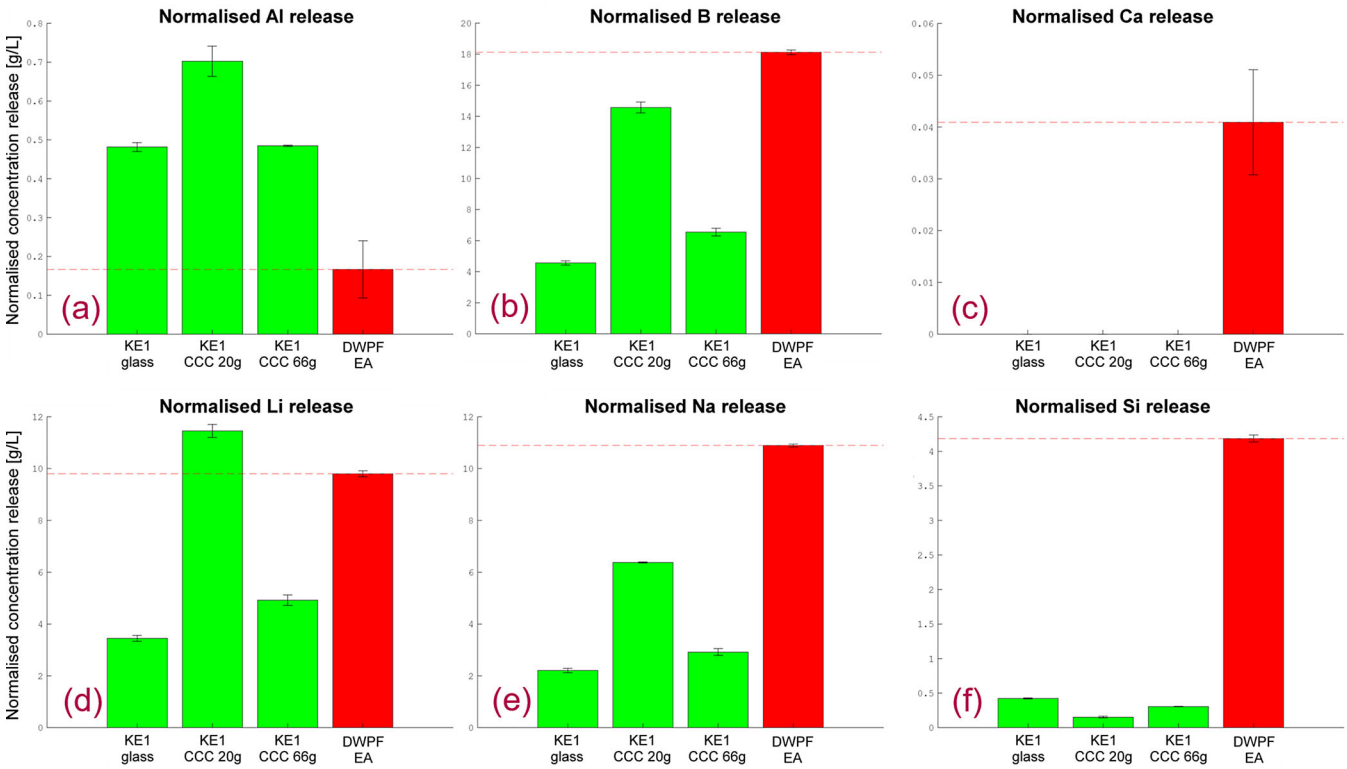

FIGURE 12 | (a)–(f) PCT ICP, normalized elemental release rates NCi for KE1_glass, KE1_CCC_20, and KE1_CCC compared to DWPF EA glass.

TABLE 12 | Normalized concentration released NCi (g/L) values of a given element normalized compared against DWPF EA NCi as a baseline to show relative increase or decrease.

NCi (g/L) vs. DWPF EA	KE1 glass	KE1 CCC (20 g)	KE1 CCC (66 g)
Al	2.89x	4.20x	2.90x
B	0.25x	0.80x	0.36x
Ca	NA	NA	NA
Li	0.35x	1.17x	0.50x
Na	0.20x	0.59x	0.27x
Si	0.10x	0.04x	0.07x

Note: Values greater than 1 indicate higher leaching compared to DWPF EA by the factor stated, while values less than 1 indicate the leaching rate is lower than DWPF EA.

glass based on its chemical durability, something that to date (with the exception of varied cooling regimes) none of the primary models discussed here and in the literature (ND, ND/OB, SM & DC) take this into account.

3.4 | Scanning Electron Microscopy

Two small monoliths of base KE1_glass and KE1_579C_4day were analyzed by both SEM and EDX. At 100x magnification (Figure 13a), a clear boundary can be seen between the crystal and glass layer. The epoxy bubbles on the right of the same image show where the sample was in contact with the platinum crucibles. Crystals grow 1–2 mm into the sample before the correct conditions for continued crystal growth are no longer present. Figure 13b shows a 2000x magnification image of the boundary area between the crystal and the glass; individual dendrites can be seen more clearly.

EDX analysis was conducted to determine the compositional differences between the base glass and different regions of the heat-treated sample. The regions of interest were the glass adjacent to nepheline crystals as well as the compositional differences between the nepheline crystals and the residual glass surrounding them.

The results of the EDX are summarized in Table 13.

The measured boron concentrations obtained by SEM-EDX are noticeably higher than the nominal values. However, these boron readings are subject to significant uncertainty due to the inherently weak boron signal, arising from its low atomic number, as well as spectral interference caused by contamination and carbon coatings, attributed to the overlap of the boron Kα (~183 eV) and the carbon Kα (~277 eV) [90].

In the above table, each row represents the following:

KE1 glass—a monolithic glass sample of KE1 simply poured and annealed without any further heat treatment, shown in Figure 6ii.

All the subsequent sample subsections are from the KE1_579C_4day sample shown in Figure 6i:

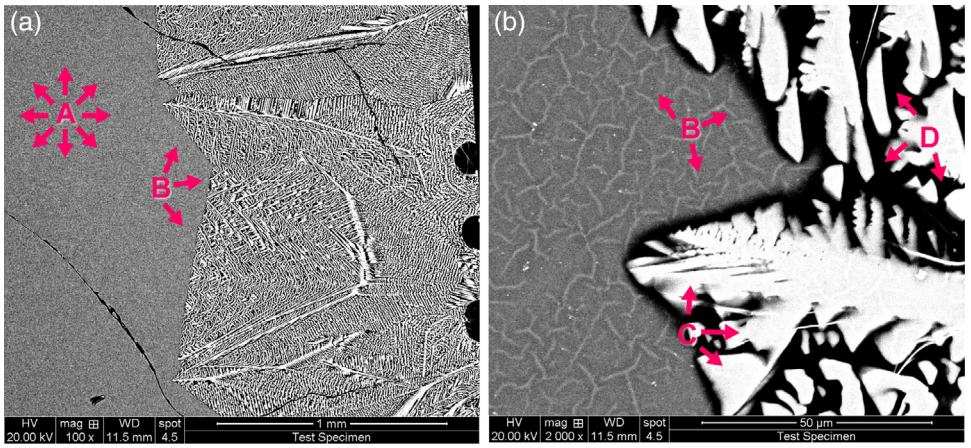

FIGURE 13 | (a) and (b)—Back scattered electron (BSE) images of Nepheline-glass interface ~1–2 mm from the platinum/sample boundary in a 4-day heat-treated sample of KE1 glass ceramic. 100x magnification (left) 2000x magnification (right). These are SEM image of the sample shown in Figure 6i.

TABLE 13 | Normalized EDX data (lithium not detected) averaged over either 60 or 80 points scans across 3 or 4 sites, with standard errors calculated for each.

Sample	Site description	B	O	Na	Al	Si	Fe	Total
KE1	**nominal wt% w/o Li**	6.47	50.22	10.76	13.23	14.40	2.10	100.00
KE1 glass	**KE1 glass (Figure 6ii)**	11.04 ± 0.22	51.86 ± 0.07	9.51 ± 0.06	12.45 ± 0.06	12.94 ± 0.06	2.20 ± 0.01	100.00
KE1 579C 4day	**Heat treated glass (Figures 6i and 13a site A)**	10.66 ± 0.19	52.68 ± 0.08	7.88 ± 0.06	12.71 ± 0.06	13.73 ± 0.08	2.34 ± 0.02	100.00
KE1 579C 4day	**Glass adjacent to crystal boundary (Figures 6i and 13a,b site B)**	11.32 ± 0.23	53.22 ± 0.11	7.32 ± 0.05	12.33 ± 0.07	13.57 ± 0.08	2.25 ± 0.02	100.00
KE1 579C 4day	**White crystal adjacent to interface (Figures 6i and 13b site C)**	0.00 ± 0.00	48.28 ± 0.11	13.88 ± 0.05	17.27 ± 0.06	19.30 ± 0.06	1.27 ± 0.03	100.00
KE1 579C 4day	**Residual glass adjacent to interface (Figures 6i and 13b site D)**	15.51 ± 0.64	59.77 ± 0.37	6.91 ± 0.11	6.74 ± 0.18	7.40 ± 0.15	3.66 ± 0.13	100.00
KE1 579C 4day	**White crystal in bulk (Figures 6i and 14a,b site E)**	0.00 ± 0.00	48.11 ± 0.06	13.97 ± 0.04	17.34 ± 0.04	19.23 ± 0.05	1.35 ± 0.06	100.00
KE1 579C 4day	**Residual glass in bulk (Figures 6i and 14a,b site F)**	17.42 ± 0.37	58.91 ± 0.23	7.26 ± 0.08	6.47 ± 0.15	7.17 ± 0.14	2.77 ± 0.11	100.00
KE1 579C 4day	**White fibers (Figures 6i and 14a,b site G)**	12.71 ± 1.64	52.83 ± 6.82	7.50 ± 0.97	6.63 ± 0.86	6.91 ± 0.89	13.42 ± 1.73	100.00

Note: The error reported is the standard error.

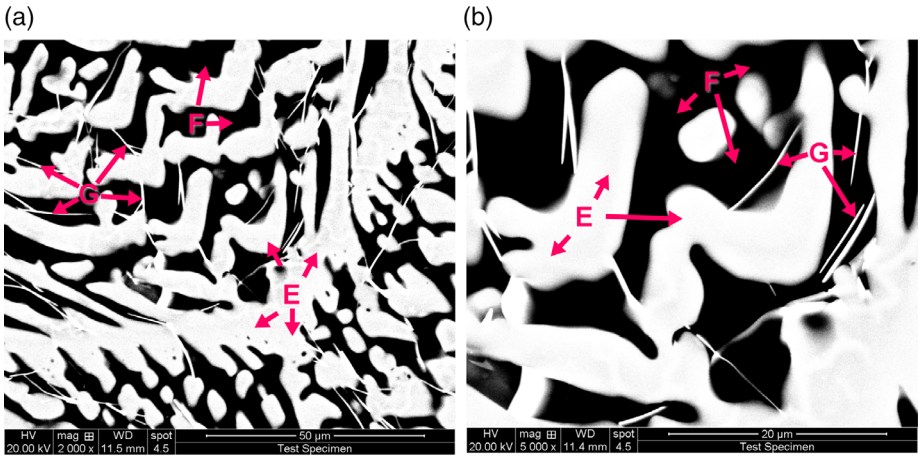

FIGURE 14 | (a) and (b) 2000x and 5000x BSE image focused on the crystalline area (white) and residual glass around it (black), away in the core of the crystal growth. Furthermore, long, narrow white formations can be seen. These are SEM image of the sample shown in Figure 6i.

Heat-treated glass—the still optically transparent glass at the center of the heat-treated sample, as far away as possible from the crystal interface. This portion of glass was approximately 1–2 mm away from the glass/crystal interface seen in the SEM images (Figure 13), as far as possible from the Pt/sample air/sample boundary as possible.

Glass adjacent to the crystal boundary—Glass directly adjacent to the crystal interface, as seen in Figure 13b at a distance of ~10–50 μm from the crystal interface.

White crystal adjacent to interface—White areas (such as those on Figure 13b) of dendritic crystals directly adjacent (~10–50 μm) to the glass crystal interface.

Residual glass adjacent to interface—Black areas (such as those on Figure 13b) surrounding dendritic crystals directly adjacent (~10–50 μm) to the glass crystal interface.

White crystals in bulk—White areas on dendritic crystals are centrally found within the crystal growth, ~0.5–1.5 mm away from both the glass crystal interface or the Pt/sample interface (such as those shown in Figure 14a,b).

Residual glass in bulk—Black areas adjacent to white dendritic crystals are centrally found within the crystal growth, ~0.5–1.5 mm away from both the glass crystal interface or the Pt/sample interface (such as those shown in Figure 14a,b).

White fibers—Slender needle-like crystals were found within the crystal structure but not the glass. These ranged 5–50 nm in length and were also analyzed by SEM. These can be seen in Figure 14a,b.

All samples were ground, polished, and carbon-coated in preparation for SEM analysis.

The EDX analysis shows that the glasses at the center of each monolith (KE1_glass and heat-treated glass) are fairly similar, with the largest relative difference being seen in the measured sodium levels. This suggests that the glass behaves in a comparably away from the Pt/sample interface, even after CCC heat treatment. Notably, the levels of the nepheline components (Na, Al, Si) did not shift by a comparable magnitude or in the same direction as each other.

When comparing KE1 glass to the heat-treated glass and the glass adjacent to the glass/crystal boundary, the main difference is the sodium being low in comparison to the original glass. The levels of boron measured increase as the boundary is approached.

The dendritic crystals adjacent to the boundary have a very similar composition to those far away from the boundary, suggesting that if nepheline forms, then it completely forms; the stoichiometry seems consistent throughout.

However, the residual glass contains more boron further away from the glass/crystal interface compared to the spot analyses closer to the interface, which is consistent with the current understanding of the issues surrounding nepheline formation. As the crystal forms, a residual borate-rich glass forms around the crystals with approximately half of the SiO_2 and Al_2O_3 (by weight) as the parent glass and around 2.5 times less SiO_2 and Al_2O_3 (by weight) when compared to the nepheline crystals.

The white fibers were rich in iron with the remaining composition being somewhat comparable to the surrounding residual glass; however, this is likely due to their thin nature (~1 μm) and the EDX taking a reading from the bulk around them due to the comparatively large excitation volume caused by the use of back scattered electrons. The iron fibers depicted in Figure 14a,b were determined to be ICDD: 01-089-5894 Iron Oxide, Maghemite (γ-$Fe_{1.966}O_{2.963}$), tetragonal space group number 96 $P4_32_12$ [91]. This was determined by XRD performed on the underside of the sample in contact with the Pt interface. The diffraction pattern showed well-defined crystalline peaks. Semi-quantitative analysis using the search and match feature on High Score Plus suggests the Pt contact interface is ~97wt% Nepheline and ~3wt% Maghemite. This phase does not readily precipitate in KE1 glass undergoing CCC heat treatment, but precipitates when held close to its crystallization exotherm (579°C) for multiple days (4 days in this instance); the phase only develops among the nepheline and

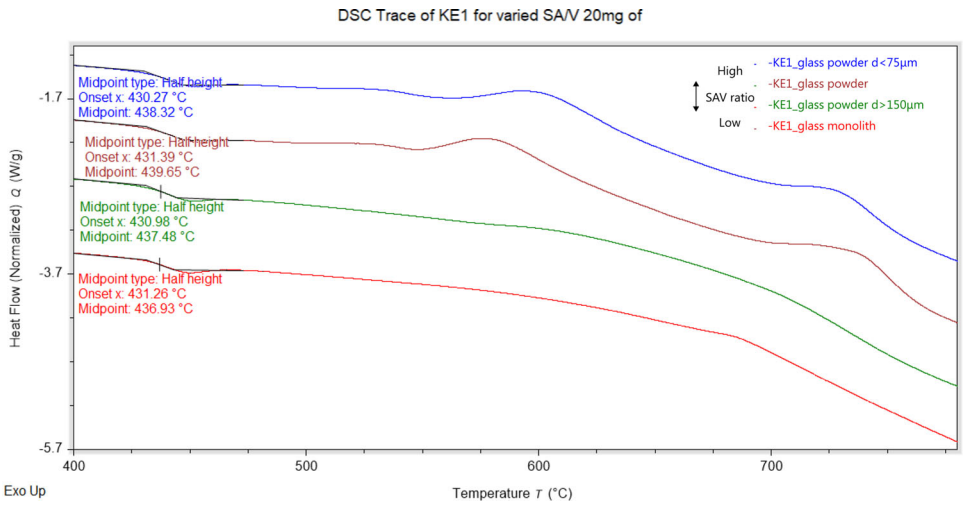

FIGURE 15 | DSC traces of four compositionally identical samples under identical experimental conditions (10°C/min in alumina pans), with almost identical glass transition behavior, but markedly different crystallization behavior due to the SA/V ratios of the samples.

adjacent borosilicate glass. This phase was not visually seen via SEM within the glass away from the Pt contact interface.

3.5 | Differential Scanning Calorimetry

DSC measurements were undertaken on 4 compositionally identical (from the same sample) KE1 glass samples. The identical (within uncertainties) T_g onset/midpoint temperature highlights that they are the same glass. The key difference in these samples is the decreasing SA/V ratio from top to bottom, which results in markedly different crystallization behavior, with the largest SA/V sample (powder filtered to less than 75 µm) showing a large exotherm, while the monolith, which has the lowest SA/V ratio of all the samples, shows no discernible exotherm (Figure 15).

4 | Evaluation

As with all CCC studies, those discussed here focus on the cooling melt along the canister centerline, thus heterogeneous nucleation due to contact with canister walls should be assumed not to be a factor. This is due to the heating rate being studied (CCC [42]) not occurring in contact with the canister wall [64]. The main instances in which the kinetics of heterogeneous nucleation become of importance are when impurities such as spinels, unmelted noble metals, or intermetallic are present.

The phase balance between spinel and nepheline has been modeled in certain compositional regions at equilibria such as along the Acmite—Nepheline join [71]. In this system, a considerable portion of the possible phase fields beneath the liquidus is comprised of phases that host both nepheline and spinels. These phases occur at temperatures starting above the typical 1150°C and are shown to exist down to temperatures at least as low as 500°C in the cited studies, a temperature range which along the canister centerline exists for multiple hours and thus likely to be somewhat representative of a system approaching equilibrium. Furthermore, in these systems, it has long been suggested that spinels have the potential to act as a nucleating surface for nepheline [59, 63, 92, 93].

This complication may be amplified by spinels growing and shrinking as they cycle between hotter and colder zones within the melter [94], making it exceedingly difficult to model second-order effects within the static laboratory crucible environment. As spinels of a certain size build up near the pour spout, it is further possible that during pouring a certain percentage makes it into the canister, at which point the melt is above T_g and below T_{liq} for an extended period of time, at which point kinetics and thermodynamics of the phases in play will determine the extent of nepheline precipitation due to heterogeneous effects.

Crystal growth from unmelted platinoids, however, can still be considered in terms of surface heterogeneous nucleation [69, 95] even if it is occurring at the bulk of the glass. This is because it is still very much limited by the amount of surface present, the energy landscape in contact with said surface, and the contact angle present with that surface; the shape and size of nucleating particle thus also matters, although incredibly hard to model.

In commercial glasses, nucleation agents may be deliberately added to increase devitrification to augment the properties of certain commercial glass ceramics. The interfaces, surfaces, or impurities often play a catalytic role, providing favorable conditions for the nucleation process and reducing the energy requirements for nucleation in a localized region.

Conditions for heterogeneous nucleation are similar to those for homogeneous nucleation; however, different surface tensions need to be considered. For instance, at the triple phase boundary (between melt, crucible wall, and atmosphere) surface tension interactions may need to be taken into account in the following way:

- The interaction between the nucleating crystal and the crucible wall.

- The surface tension between the germinating nucleus attempting to push against the melt.
- The surface tension between the germinating nucleus and the crucible wall.
- The surface tension between the germinating nucleus and the atmosphere.
- Furthermore, surface interactions among the crucible, melt, and atmosphere at the triple-phase boundary may need to be considered.
- Any angles formed between the tension forces in question.

Even in the simplest case where assumptions about nuclei being spherical are held, this will result in a considerably more complex set of parameters; nevertheless, nucleation rate can be expressed by a similar equation to that for the homogeneous case:

$$\mathrm{I(T)_{het}} = \mathrm{n \cdot f \cdot \exp\left(-\frac{W_*^{het}(\theta)}{k_B T}\right) \cdot \exp\left(-\frac{\Delta E_D}{k_B T}\right)} \quad (5)$$

Equation (5)—**For the nucleation rate, with two key terms representing the two barriers to nucleation that need to be overcome**.

Where the atoms per unit volume (n) and the frequency of atomic vibrations (f) are multiplied by two Boltzmann probability factors, each representing a barrier to nucleation which needs to be overcome, the first dominated by the thermodynamic barrier W^*, and the second is the kinetic barrier ΔE_D.

In the heterogeneous case, $W^*_{het}(\theta)$ can be simplified to be a function of a contact angle theta and depend upon multiple surface tensions between different boundaries [95, 96].

In the case where a partial sphere is being considered to nucleate within the melt against a crucible wall, it can be shown that the heterogeneous nucleation can be simplified to the homogeneous nucleation rate multiplied by a geometric term. In this most simple of heterogeneous cases, the critical radius r^* is the same as in the homogeneous case $r^* = \frac{2\gamma}{\Delta G_x}$, where G_x is the reduction in Gibbs Free Energy as a result of forming a nucleus (crystallization) and γ is equivalent to the net change in Gibbs Free Energy per unit area.

$$\mathrm{W_*^{het}} = \frac{16\pi\gamma^3}{3\Delta G_3^x} \cdot \left[\frac{1}{4}(1-\cos\theta)^2 \cdot (2+\cos\theta)\right] \quad (6)$$

$$= \mathrm{W_*^{homo}}\left[\frac{1}{4}(1-\cos\theta)^2 \cdot (2+\cos\theta)\right] \quad (6)$$

Equation (6)—**For the heterogeneous thermodynamic barrier W* as a function of contact angle θ.**

Alternatively, when $\theta = \pi$rad then $\mathrm{W_*^{het}} = \mathrm{W_*^{homo}}$, which is the case when the wall is offering no aid to nucleation whatsoever. Thus, depending on the size of the thermodynamic (W^*) and kinetic barriers ($\Delta \mathrm{E_D}$), a surface can make a considerable difference to the nucleation rate; however, this is something that is very hard to quantify, but may be experimentally tested.

While classical nucleation theory assumes the contact angle is constant, if any nucleating agents are present, while the poured canister is fluid enough, these will be under the effect of gravity, as these are often denser than the melt. Furthermore, during the pour, the viscous glass fluid cannot be static by definition.

The kinetic barrier (ΔE_D) is the activation energy (energy required for the chemical reaction to occur) needed to begin the formation of a crystal nucleus. This is the energy necessary to overcome the crystal-liquid interface and the breaking and realignment of bonds into the more ordered structure of the crystalline nucleus. This component of the nucleation Equation (5) will be somewhat static and predictable.

Conversely, the thermodynamic barrier ($\mathrm{W^*}$) on the other hand is the energy required to form a stable nucleus with a critical radius that minimizes the system's Gibbs Free Energy, so that it is lower than the alternative of re-dissolving into the liquid state. This becomes a function of a tendentially varying contact angle. At the very least, due to the non-uniform shape and size of spinels and un melted platinoids, it can be said that this component would not be comparable to the interface of a platinum crucible surface, even if just for the amount of surface area present. At this juncture, it simply becomes about how prominent this component of the equation becomes to decide whether the experimental setup is measurably different from the expected value of a real-world canister melt.

It is very much possible to find instances where photographic records have been kept of CCC samples in which clear evidence of contact surface nucleation with the crucible can be seen, with examples by Russel et al. [97–99] and Lonergan et al. [100] being among the most readily discernible, thanks to the excellent recordkeeping in their reports. These examples are using both platinum and fused silica crucibles. It might be expected that fused silica crucibles would have a low level of glass/liquid interaction, as at the relatively low melt and heat treatment temperatures of HLW, fused silica should be a very viscous fluid, neither leaching into the melt nor providing it with a solid surface, but this is apparently not always the case.

The subsequently reported crystal fractions of these samples, much like those in the present study, will be an average of the entire volume of glass ceramic made. This will be comprised of a high crystal fraction, low volume area around the contact interface, and a higher volume glass with essentially a crystal fraction of either zero or close to zero, which is representative of what would occur on the canister centerline (the core of the sample). In models where the presence of nepheline under CCC conditions is recorded as a Boolean (1s or 0s), it is not hard to envision how this is a considerable problem. Further complications will be introduced based on how these samples are sectioned. If the whole sample is powdered for various techniques such as XRD, compositional analysis, and PCT, the results, especially the PCT and XRD, may be different than if these are first sectioned and then sent off and powdered individually. Alternatively, some researchers may choose to simply use the particle size fractions not used for PCT for XRD and compositional analysis.

Muller et al. [101] noted a relatively similar phenomenon to that showcased by the KE1_579C_4day sample in this research. The

referenced report discusses a sample LAWB53FCC, a relatively complex sodium boro-aluminosilicate glass containing over 10 oxide components as well as Cl and F, which was melted at 1150°C for 4hours after a slow ramp. Following this, it was not stirred, and the canister was cooled (in accordance with the LAW schedule, which will differ from the CCC thermal profile discussed throughout this document). The sample was divided into three parts: top, middle, and bottom, and it is noted that only the bottom portion contained pyroxene crystals. SEM imagery shows the crystals nucleating at the platinum contact interface in almost identical fashion to the nepheline seen in this study.

The KE1 glass composition was designed as an entry point to the study of the low accuracy nepheline crystallization prediction space. It was designed to broadly represent the nuclear waste glass situated on the fault line between compositions that do and do not precipitate nepheline, while being simple enough to study without excessively complex interactions between a double-digit number of oxides.

Multiple experiments were designed around the KE1 glass to test the extent to which SA/V effects could be used in an effort to alter the results of crystalline quantification and industry standard durability tests, and thus explain why the nepheline predictor models to date might be overly conservative.

Shaharyar et al. [61] showed that relatively minor compositional changes can alter the mode of nucleation from surface (2D) to bulk (3D) or vice versa as determined by the Avrami exponent [78–80], the idea of a well-defined boundary between compositions that do and do not precipitate nepheline under a fixed thermal profile (CCC) is plausible but inevitably complex. Due to the severely complicated nature of the 15–40 or more oxide compositions in nuclear waste glass, this would likely be a highly non-linear boundary to predict, as is seen with the modeling of many other glass properties (crystallization as seen by the models discussed herein [47, 49, 50], durability [102], glass transition [103], liquidus [104], viscosity [105] to name just a few).

McClane et al. [51] even suggest controlling the mode of nucleation by limiting it to 2D growth only as a potential strategy for combatting problematic nepheline devitrification. Furthermore, the nucleation and growth of stable spinels can also be promoted or suppressed by compositional changes [70] and therefore, if a cooling melt simply requires a nucleating phase to grow from, this could add further complexity to the determination of a nepheline boundary.

Since these incredibly complex relationships exist, there is merit in attempting to use advanced mathematical techniques [50, 53, 106] to deconvolute the task, and these have shown an ever-increasing degree of merit; however, they will also be limited by any inherent data-based flaws that are fed into the models, such as those identified in this study.

The optical micrographs, SEM images, X-ray diffraction patterns, as well as the DSC traces clearly show a not insignificant effect of SA/V on crystallization and consequent result on dissolution tests, strongly suggesting that these compositions' primary crystallization mechanism is heterogeneous surface nucleation as experimentally verified by the Avrami constant of $n = 1.51 \pm 0.25$.

Reactions between glass and platinum are known to occur [68], yet due to being one of the most inert materials, they are often assumed to be negligible and ignored. It is not uncommon for images in literature to clearly show crystallization at the platinum contact interface [97–100] or the phenomenon of surface-specific crystal growth to be discussed [51]. When subsequently these are powdered and prepared for PCT, the average of the whole sample, the surface (that in contact with the platinum), and the bulk (which would actually be more representative of the canister CCC area), which has often not crystallized now represent the durability datapoint for this composition within the nepheline database, which may not be a true representation.

The growth of Maghemite crystals on the KE1_579_C sample among the nepheline crystals and the residual glass (but not within the glass core of the sample away from the platinum contact interface) over the course of 4 days implies that a sample which has gone undergone CCC has not reached phase equilibrium even though it has been gradually cooled over the course of many hours and is thus just a snapshot of the path toward said equilibrium. The models currently being used suggest that composition plays the sole role in the transformation toward equilibrium, which is ultimately frozen in by a CCC temperature profile. This research suggests that while the role of composition is important and critical to understand, SA/V effects are influencing the rate toward the ultimate equilibrium at the contact interface, thus potentially making these tests not wholly representative of real-world canister melts.

In this case, this translates to the experimental setup being a key determining factor as to whether the glass fails or passes a durability comparison with DWPF EA glass; a critical go/no go decision for the manufacture of nuclear waste glass [29, 31]. All the models to date only take the composition of the glass into account, and no other experimental variables, such as the SA/V ratio.

This is exceedingly important when we consider that along the canister centerline, where the slow cooling kinetics favor nepheline crystallization, there is no large nucleating surface to aid in the precipitation of nepheline (barring any un-melted platinoids or precipitated spinels), something which, conversely, is present in every single experimental sample within the NP database (the Pt crucible wall). Nepheline prediction models are often described as being overly conservative [6, 45–47, 49, 50]. This study postulates that every model to date is overly conservative because every single datapoint relied upon has a substantial aid to nucleation that is not present in real-world canister centerline conditions. False positives and false negatives found in the low accuracy regions could potentially be due to variation in nucleation mechanism and SA/V of the sample to the platinum wall; however, further research is required to verify this.

The variation in phases precipitated by isothermal heat treatment and CCC heat treatment in this study, while all are suspected of being detrimental to chemical durability [88], provides further evidence of the delicate balance of chemical forces within the

glass during devitrification, with varied treatments directing the system along distinct crystallization pathways.

A collaborative 2011 study [107] showed that non-trivial differences can be obtained when implementing the same experimental methods (liquidus temperature measurements on nuclear waste glasses) by different researchers at different labs, even when samples are tightly controlled (all made at one institution and sent out). Further complexity would be added if individual research institutions were independently preparing the samples, potentially using different raw materials and compounding differences further. This will no doubt exacerbate the size of the errors in the values listed in the database.

Lastly, as SA/V parameters for all samples may be inconsistent throughout the nepheline CCC database and often not recorded in literature (although certain instances where this is done to some extent can be found [65]), with factors such the extent of homogeneous versus heterogenous crystal growth (Avrami exponent) for each composition being highly non-linear further training on the database may still be limited even if more compositions are added to it. McClane et al. [51] derived similar Avrami constant values in nepheline-bearing samples, which also showed contact interface growth, similar to those in this study ($n = 1.51$ in this study compared to $n = 1.28–2.05$). 1D-2D crystal growth can be explained as the dendritic habit of nepheline [27, 108, 109] manifests in needle-like crystal growth (1D), which fan out, eventually impinge on one another, and intersect as they grow, forming two-dimensional dendritic crystals (2D). This highlights the need to focus more on property-based models [17] that link the measurable physical or chemical properties to the predicted outcomes.

Future research needs to focus on quantifying the extent of the heterogeneous nucleation, forecasting and modeling it to account for the lack of a nucleating surface within the cannister, and attempting to determine whether the false negatives and false positives along the prediction boundary are caused by a change in mode of nucleation from heterogeneous to homogeneous or vice versa. This can be done by more accurately calculating the glass SA/V ratio and the resultant effects of glass crucible interactions by studying more than just the two data points collected in this study. Better understanding of the mode of nucleation (Avrami exponent), phase kinetics, coordination, and redox state of the various compositions may all be critical to the path forward with this research.

Furthermore, going forward, the stipulation of a minimum SA/V ratio for CCC samples prepared for PCT and the core drilling of samples to avoid glass within a predefined distance of the surface to omit any irrelevant effects from surface interactions would be beneficial. What the SA/V and the edge distance requirements should be needs to be determined from further investigation.

5 | Conclusion

Surface area effects have either plagued or benefited scientists for centuries; Wolfgang Pauli is famous for stating, *"God made the bulk; surfaces were invented by the devil"* [110]. In this instance, this holds true as bulk predictions necessary for this work are being stifled by the hard-to-quantify interactions caused by the lab-scale interactions with surfaces.

Nepheline prediction models are often described as being overly conservative, as the models limit waste loading below what would be possible in real-world canister melts. While this has often been discussed as either a data limitation (more glass compositions are needed for study) or a model complexity issue (non-linear dependencies limit the predictive abilities of the models), this study suggests that experimental limitations are at least partly to blame.

Every sample within the Nepheline CCC prediction database has been made on a laboratory scale, a relatively large nucleating surface is always present in these experiments (the crucible wall), something which by definition cannot be present along the canister centerline. Thus, compositions in the Nepheline CCC database will crystallize more readily than real-world canister pours. In this study, the effects of SA/V variability have been demonstrated using a variety of techniques on both crystallization and durability.

Acknowledgments

Jack D. Cornwall would like to express his deepest gratitude to his children, Maisie, Evie, and Noah, for their continued and constant encouragement; to his wife, Louise, and his parents, for supporting his studies. Thank you to all the technical staff who trained him to a high level of competency and supported him in the use of the experimental techniques used in this work. Thank you to Dr. Erhan Kilinc for the many hours of invaluable ad hoc support. Thank you to his cohort of close peers and soon-to-be Drs. Casey Walsh, Miu Onaru, Hannah Blystra, and Luke Cooper, for suffering through this with him. Thank you to his supervisors for supervising and his funders for funding.

Funding

This research was cofounded by Sheffield Hallam University and the U.S. Department of Energy (DOE) Waste Treatment and Immobilization Plant Project.

Data Availability Statement

The data that support the findings of this study are available from U.S. Department of Energy. Restrictions apply to the availability of these data, which were used under license for this study. Data are available from the author(s) with the permission of U.S. Department of Energy. For the purpose of open access, the author has applied a Creative Commons Attribution (CC BY) licence to any Author Accepted Manuscript version of this paper, arising from this submission.

Endnotes

[1]Where errors have been stated, they are the standard errors based on three repeat runs and do not represent the comprehensive error for the technique, nor do the decimal places represent the achievable level of accuracy for a given instrument.

References

1. C. L. Thorpe, J. J. Neeway, C. I. Pearce, et al., "Forty Years of Durability Assessment of Nuclear Waste Glass by Standard Methods," *NPJ Materials Degradation* 5, no. 1 (2021): 61, https://doi.org/10.1038/s41529-021-00210-4.

2. J. A. C. Marples, "The Preparation, Properties, and Disposal of Vitrified High Level Waste From Nuclear Fuel Reprocessing," *Glass Technology* 29, no. 6 (1988): 230–247.

3. S. Peuget, J.-N. Cachia, C. Jégou, et al., "Irradiation Stability of R7T7-Type Borosilicate Glass," *Journal of Nuclear Materials* 354, no. 1–3 (2006): 1–13, https://doi.org/10.1016/j.jnucmat.2006.01.021.

4. S. V. Stefanovsky, M. V. Skvortsov, O. I. Stefanovsky, et al., "Preparation and Characterization of Borosilicate Glass Waste Form for Immobilization of HLW From WWER Spent Nuclear Fuel Reprocessing," *MRS Advances* 2, no. 11 (2017): 583–589, https://doi.org/10.1557/adv.2016.622.

5. H. K. Manaktala, "An Assessment of Borosilicate Glass as a High-Level Waste Form" (1992), accessed May 4, 2026, https://www.nrc.gov/docs/ml0336/ml033650021.pdf.

6. A. Goel, J. S. McCloy, R. Pokorny, and A. A. Kruger, "Challenges With Vitrification of Hanford High-Level Waste (HLW) to Borosilicate Glass—An Overview," *Journal of Non-Crystalline Solids X* 4 (August 2019): 100033, https://doi.org/10.1016/j.nocx.2019.100033.

7. J. Anderson, "Hanford Cleanup: DOE Should Validate Its Analysis of High-Level Waste Treatment Alternatives" (2023), accessed: May 4, 2026, https://www.gao.gov/assets/gao-23-106093.pdf.

8. J. Marcial, B. J. Riley, A. A. Kruger, C. E. Lonergan, and J. D. Vienna, "Hanford Low-Activity Waste Vitrification: A Review," *Journal of Hazardous Materials* 461, no. 132437 (2024), https://doi.org/10.1016/j.jhazmat.2023.132437.

9. W. F. Hamel, L. K. Holton, and I. L. Pegg, "Performance Enhancements to the Hanford Waste Treatment and Immobilization Plant Low-Activity Waste Vitrification System TARGETED IMPROVEMENTS TO INCREASE LAW VITRIFICATION CAPABILITY LAW Glass Waste Loading Improvements," in Proceedings of the Waste Management Symposia (WM Symposia Inc., 2006), https://www.osti.gov/biblio/21208595.

10. I. Joseph, B. W. Bowan II, and H. Gan, et al. *High Aluminum HLW Glasses for Hanford's WTP ORP-42448-FP* (WM Symposia, 2010), 1–13, https://www.osti.gov/biblio/969813.

11. R. L. Russell, V. Gervasio, X. Lu, et al., "Expansion of the Direct Feed High-Level Waste Glass Composition in the High Al Range," (U.S. Department of Energy, Office of Scientific and Technical Information [OSTI], 2025), https://doi.org/10.2172/3000232.

12. D. Kim, M. J. Schweiger, C. P. Rodriguez, et al., "Formulation and Characterization of Waste Glasses With Varying Processing Temperature," (U.S. Department of Energy, Office of Scientific and Technical Information [OSTI], 2011), https://doi.org/10.2172/1028572.

13. J. D. Vienna, D. S. Kim, M. J. Schweiger, G. F. Piepel, J. O. Kroll, and A. A. Kruger, "Glass Formulation and Testing for U.S. High-Level Tank Wastes Project 17210 Year 1 Status Report: October 15, 2014," (Pacific Northwest National Laboratory, 2014), pp. 1–10, http://www.hanford.gov/files.cfm/Glass_Formulation_Year_1_Report_Final_10-15-14,_PNNL-SA-84872.pdf.

14. H. Li, J. D. Vienna, P. Hrma, D. E. Smith, and M. J. Schweiger, "Nepheline Precipitation in High-Level Waste Glasses : Compositional Effects and Impact on the Waste Form Acceptability," *MRS Proceedings* 465 (September 1996): 261, https://doi.org/10.1557/PROC-465-261.

15. H. Esmat and E. Emad, "Preparation of Nepheline Glass–Ceramics for Dental Applications," *Materials Chemistry and Physics* 112, no. 2 (2008): 0254–0584, https://doi.org/10.1016/j.matchemphys.2008.05.079.

16. H. Li, P. Hrma, J. D. Vienna, M. Qian, Y. Su, and D. E. Smith, "Effects of Al_2O_3, B_2O_3, Na_2O, and SiO_2 on Nepheline Formation in Borosilicate Glasses: Chemical and Physical Correlations," *Journal of Non-Crystalline Solids* 331, no. 1–3 (2003): 202–216, https://doi.org/10.1016/j.jnoncrysol.2003.08.082.

17. A. Deshkar, B. Parruzot, R. E. Youngman, O. Gulbiten, J. D. Vienna, and A. Goel, "Compositional Dependence of Crystallization and Chemical Durability in Alkali Aluminoborosilicate Glasses," *Journal of Non-Crystalline Solids* 590 (March 2022): 121694, https://doi.org/10.1016/j.jnoncrysol.2022.121694.

18. J. Marcial, J. Crum, O. Neill, and J. McCloy, "Nepheline Structural and Chemical Dependence on Melt Composition," *American Mineralogist* 101, no. 2 (2016): 266–276, https://doi.org/10.2138/am-2016-5370.

19. K. M. Fox, et al., "International Study of Aluminum Impacts on Crystallization in U.S. High Level Waste Glass" (Pacific Northwest National Laboratory, 2008).

20. C. E. Lonergan, J. O. Kroll, C. H. Skidmore, Z. J. Nelson, and J. D. Vienna, "X-Ray Diffraction and Product Consistency Test Results for the Phase 6 Study of Nepheline Formation in High-Level Waste Glasses" (Pacific Northwest National Laboratory, 2019).

21. A. B. Harker and D. R. Clarke, "Dissolution Mechanisms in High-Level Nuclear Waste Consolidation Forms" (Pacific Northwest National Laboratory, 1982).

22. J. M. Perez and J. H. Westsik, "Effects of Cracks on Glass Leaching," *Nuclear and Chemical Waste Management* 2, no. 2 (January 1981): 165–168, https://doi.org/10.1016/0191-815X(81)90034-6.

23. D. W. Faletti and L. J. Ethridge, "A Method for Predicting Cracking in Waste Glass Canisters," *Nuclear and Chemical Waste Management* 8, no. 2 (January 1988): 123–133, https://doi.org/10.1016/0191-815X(88)90071-X.

24. J. V. Crum, L. A. Turo, B. J. Riley, M. Tangmcclo, A. Kossoy, and K. E. Sickafus, "Glass Ceramic Waste Forms for Combined CS + LN + TM Fission Products Waste Streams," (U.S. Department of Energy, Office of Scientific and Technical Information (OSTI), 2010), https://doi.org/10.2172/1048015.

25. P. R. Hrma and G. F. Piepel, "Property/Composition Relationships for Hanford High-Level Waste Glasses Melting at 1150C," (U.S. Department of Energy, Office of Scientific and Technical Information (OSTI), 1994), https://doi.org/10.2172/10121752.

26. P. R. Hrma, "Towards Optimization of Nuclear Waste Glass: Constraints, Property Models, and Waste Loading," in 96th Annual Meeting of the American Ceramic Society (American Ceramic Society, 1994), https://www.osti.gov/biblio/10167209.

27. J. S. McCloy and S. Schuller, "Vitrification of Wastes: From Unwanted to Controlled Crystallization, a Review," *Comptes Rendus Géoscience, Glas an ubiquitous Mater* 354, no. S1 (2022): 121–160, https://doi.org/10.5802/crgeos.111/.

28. B. J. Riley, J. A. Rosario, and P. Hrma, "Impact of HLW Glass Crystallinity on the PCT Response," (U.S. Department of Energy, Office of Scientific and Technical Information (OSTI), 2002), http://www.osti.gov/scitech/servlets/purl/15001115.

29. ASTM International *Standard Test Methods for Determining Chemical Durability of Nuclear, Hazardous, and Mixed Waste Glasses and Multiphase Glass Ceramics : The Product Consistency Test (PCT)* (ASTM International, 2021), https://doi.org/10.1520/C1285-21.

30. C. Jantzen, N. Bibler, D. Beam, C. Crawford, and M. Pickett, "Characterisation of the Defense Waste Processing Facility (DWPF) Environmental Assessment (EA) Glass Standard Reference Material," (U.S. Department of Energy, Office of Scientific and Technical Information (OSTI), 1993), https://www.osti.gov/servlets/purl/10173249.

31. United States Department of Energy, "Waste Acceptance Product Specification for Vitrified High-Level Waste Forms," (U.S. Department of Energy, Office of Scientific and Technical Information (OSTI), 1993), https://www.nrc.gov/docs/ML0335/ML033560152.pdf.

32. ASTM International *Standard Test Method for Static Leaching of Monolithic Waste Forms for Disposal of Radioactive Waste* (ASTM International, 2021), https://doi.org/10.1520/C1220-21.

33. ASTM International *Standard Test Method for Measuring Waste Glass or Glass Ceramic Durability by Vapor Hydration Test* (ASTM International, 2024), https://doi.org/10.1520/C1663-24.

34. Environmental Protection Agency *Toxicity Characteristic Leaching Procedure* (Environmental Protection Agency, 1992), https://www.epa.gov/sites/default/files/2015-12/documents/1311.pdf.

35. R. L. Russell, K. S. Matlack, T. L. Taylor, and B. J. Riley, "Glass Compositions and Properties of Enhanced Waste Glass With High Alumina Content for High-Level Waste," (Pacific Northwest National Laboratory, 2018), https://www.pnnl.gov/publications/glass-compositions-and-properties-enhanced-waste-glass-high-alumina-content-high-level.

36. J. Reiser, E. Cordova, S. Cooley, J. Neeway, J. Vienna, and B. Parruzot, "Product Consistency Test and Vapor Hydration Test Comparisons of a Radioactive Hanford Waste Glass With Its Non- Radioactive Simulant Glass," (Pacific Northwest National Laboratory, 2023), https://doi.org/10.2172/1998870.

37. T. Jin, M. A. Hall, J. D. Vienna, et al., "Glass-Contact Refractory of the Nuclear Waste Vitrification Melters in the United States: A Review of Corrosion Data and Melter Life," *International Materials Reviews* 68, no. 8 (2023): 1135–1157, https://doi.org/10.1080/09506608.2023.2211469.

38. P. E. Mariner, W. P. Gardner, G. E. Hammond, S. D. Sevougian, and E. R. Stein, "Application of Generic Disposal System Models," (U.S. Department of Energy, 2015), https://www.energy.gov/sites/prod/files/2016/02/f29/126ApplicatGenericDisposSystModelsGDSA.pdf.

39. United States. Department of Energy, "Assessment of Disposal Options for DOE-Managed High-Level Radioactive Waste and Spent Nuclear Fuel" (U.S. Department of Energy, 2014) https://www.energy.gov/ne/articles/assessment-disposal-options-doe-managed-high-level-radioactive-waste-and-spent-nuclear.

40. D. P. Guillen, "Thermal Predictions of the Cooling of Waste Glass Canisters," *Transactions of the American Nuclear Society* 111 (2014): 1511–1514.

41. C. P. Rodriguez, J. Chun, J. V. Crum, et al., "Thermal Properties of Simulated Hanford Waste Glasses," *Journal of the American Ceramic Society* 100, no. 6 (2017): 2533–2542, https://doi.org/10.1111/jace.14786.

42. L. Petkus, *Canister Centerline Cooling Data, Revision 1* (River Protection Project, 2003).

43. E. M. Levin, H. F. McMurdie, and F. P. Hall, *Phase Diagrams for Ceramists* (American Ceramic Society, 1956), https://doi.org/10.1111/j.1151-2916.1949.tb19765.x.

44. J. F. Schairer and N. L. Bowen, "Melting Relations in the Systems Na_2O-Al_2O_3-SiO_2 and K_2O-Al_2O_3-SiO_2," *American Journal of Science* 245, no. 4 (April 1947): 193–204, https://doi.org/10.2475/ajs.245.4.193.

45. K. M. Fox, T. B. Edwards, and D. K. Peeler, "Control of Nepheline Crystallization in Nuclear Waste Glass," *International Journal of Applied Ceramic Technology* 5, no. 6 (2008): 666–673, https://doi.org/10.1111/j.1744-7402.2008.02250.x.

46. J. O. Kroll, Z. J. Nelson, C. H. Skidmore, D. R. Dixon, and J. D. Vienna, "Formulation of High-Al_2O_3 Waste Glasses From Projected Hanford Waste Compositions," *Journal of Non-Crystalline Solids* 517 (February 2019): 17–25, https://doi.org/10.1016/j.jnoncrysol.2019.05.001.

47. J. S. McCloy, M. J. Schweiger, C. P. Rodriguez, and J. D. Vienna, "Nepheline Crystallization in Nuclear Waste Glasses: Progress Toward Acceptance of High-Alumina Formulations," *International Journal of Applied Glass Science (IJAGS)* 2, no. 3 (2011): 201–214, https://doi.org/10.1111/j.2041-1294.2011.00055.x.

48. C. P. Rodriguez, J. S. McCloy, M. J. Winschell, and A. Schweiger, "Optical Basicity and Nepheline Crystallization in High Alumina Glasses," (U.S. Department of Energy – Office of Scientific and Technical Information (OSTI), 2011): 92, https://doi.org/10.2172/1019213.

49. J. D. Vienna, J. O. Kroll, P. R. Hrma, J. B. Lang, and J. V. Crum, "Submixture Model to Predict Nepheline Precipitation in Waste Glasses," *International Journal of Applied Glass Science (IJAGS)* 8, no. 2 (June 2017): 143–157, https://doi.org/10.1111/ijag.12207.

50. I. Sargin, C. E. Lonergan, J. D. Vienna, J. S. McCloy, and S. P. Beckman, "A Data-Driven Approach for Predicting Nepheline Crystallization in High-Level Waste Glasses," *Journal of the American Ceramic Society* 103, no. 9 (2020): 4913–4924, https://doi.org/10.1111/jace.17122.

51. D. L. McClane, J. W. Amoroso, K. M. Fox, and A. A. Kruger, "Nepheline Crystallization Behavior in Simulated High-Level Waste Glasses," *Journal of Non-Crystalline Solids* 505 (February 2019): 215–224, https://doi.org/10.1016/j.jnoncrysol.2018.11.018.

52. T. J. Menkhaus, P. Hrma, and H. Li, "Kinetics of Nepheline Crystallization From High-Level Waste Glass," *Ceramic Transactions* 107 (1999): 461–469.

53. I. Sargin, J. S. McCloy, and S. P. Beckman, "Multivariate Analysis: An Essential for Studying Complex Glasses," *Journal of the American Ceramic Society* 105, no. 12 (2022): 7196–7210, https://doi.org/10.1111/jace.18657.

54. S. Lee, P. Hrma, R. Pokorny, et al., "Effects of Alumina Sources (Gibbsite, Boehmite, and Corundum) on Melting Behavior of High-Level Radioactive Waste Melter Feed," *MRS Advances* 2, no. 11 (2017): 603–608, https://doi.org/10.1557/adv.2016.644.

55. J. C. Rigby, D. R. Dixon, D. A. Cutforth, et al., "Melting Behaviour of Simulated Radioactive Waste as Functions of Different Redox Iron-Bearing Raw Materials," *Journal of Nuclear Materials* 569, no. 5 (October 2022): 153946, https://doi.org/10.1016/j.jnucmat.2022.153946.

56. J. Marcial, J. Kloužek, M. Vernerová, et al., "Effect of Al and Fe Sources on Conversion of High-Level Nuclear Waste Feed to Glass," *Journal of Nuclear Materials* 559 (2022): 153423, https://doi.org/10.1016/j.jnucmat.2021.153423.

57. M. Eret, L. Löwy, J. Kloužek, et al., "Effect of Alumina Source on the Retention of Rhenium During Low-Activity Waste Feed Conversion to Glass," *Ceramics International* 50, no. 21 (2024): 42229–42236, https://doi.org/10.1016/j.ceramint.2024.08.067.

58. J. D. Eales, A. M. T. Bell, D. A. Cutforth, A. A. Kruger, and P. A. Bingham, "Structural Changes in Borosilicate Glasses as a Function of Fe_2O_3 Content: A Multi-Technique Approach," *Journal of Non-Crystalline Solids* 622 (April 2023): 122664, https://doi.org/10.1016/j.jnoncrysol.2023.122664.

59. J. McCloy, N. Washton, P. Gassman, J. Marcial, J. Weaver, and R. Kukkadapu, "Nepheline Crystallization in Boron-Rich Alumino-Silicate Glasses as Investigated by Multi-Nuclear NMR, Raman, & Mössbauer Spectroscopies," *Journal of Non-Crystalline Solids* 409 (2015): 149–165, https://doi.org/10.1016/j.jnoncrysol.2014.11.013.

60. J. Marcial, O. K. Neill, M. Newville, J. V. Crum, and J. McCloy, "Effect of Cooling Profile on Crystalline Phases, Oxidation State, and Chemical Partitioning of Complex Glasses," *MRS Advances* 5, no. 11 (February 2020): 569–579, https://doi.org/10.1557/adv.2020.89.

61. Y. Shaharyar, J. Y. Cheng, E. Han, et al., "Elucidating the Effect of Iron Speciation (Fe^{2+}/Fe^{3+}) on Crystallization Kinetics of Sodium Aluminosilicate Glasses," *Journal of the American Ceramic Society* 99, no. 7 (2016): 2306–2315, https://doi.org/10.1111/jace.14239.

62. R. Pokorny and P. Hrma, "Mathematical Modeling of Cold Cap," *Journal of Nuclear Materials* 429, no. 1–3 (October 2012): 245–256, https://doi.org/10.1016/j.jnucmat.2012.06.013.

63. A. Deshkar, M. Ahmadzadeh, A. Scrimshire, et al., "Crystallization Behavior of Iron- and Boron-Containing Nepheline ($Na_2O{\cdot}Al_2O_3{\cdot}2SiO_2$) Based Model High-Level Nuclear Waste Glasses," *Journal of the American Ceramic Society* 102, no. 3 (2019): 1101–1121, https://doi.org/10.1111/jace.15936.

64. D. L. McClane, J. W. Amoroso, K. M. Fox, M. C. Hsieh, M. R. Kesterson, and A. A. Kruger, "Nepheline Crystallization and the Residual Glass Composition: Understanding Waste Glass Durability," *International Journal of Applied Glass Science (IJAGS)* 11, no. 4 (2020): 649–659, https://doi.org/10.1111/ijag.15418.

65. J. Kroll, J. Vienna, Z. Nelson, and C. Skidmore, "Results From Phase 5 Study on Nepheline Formation in High-Level Waste Glasses Containing High Concentrations of Alumina," (U.S. Department of Energy, Office of Scientific and Technical Information (OSTI), July 2018), https://doi.org/10.2172/1478423.

66. D. Kim, J. D. Vienna, D. K. Peeler, et al., "Improved Alumina Loading in High-Level Waste Glasses," in Proceedings of the WM2008 Conference, Phoenix, AZ, USA, Feb. 24–28, 2008, 8460.

67. D. S. Kim, J. D. Vienna, P. Hrma, et al., "Development and Testing of ICV Glasses for Hanford LAW," (Pacific Northwest National Laboratory, 2003).

68. J. H. Cowan, "Platinum-Glass Reactions," Proceedings of the 42nd Conference on Glass Problems: Ceramic Engineering and Science Proceedings (1982): 218–228, https://doi.org/10.1002/9780470318744.ch12.

69. J. Alton, T. J. Plaisted, and P. Hrma, "Kinetics of Growth of Spinel Crystals in a Borosilicate Glass," *Chemical Engineering Science* 57, no. 13 (July 2002): 2503–2509, https://doi.org/10.1016/S0009-2509(02)00121-5.

70. C. M. Jantzen and K. G. Brown, "Predicting the Spinel-Nepheline Liquidus for Application to Nuclear Waste Glass Processing. Part I: Primary Phase Analysis, Liquidus Measurement, and Quasicrystalline Approach," *Journal of the American Ceramic Society* 90, no. 6 (2007): 1866–1879, https://doi.org/10.1111/j.1551-2916.2006.01027.x.

71. C. M. Jantzen and K. G. Brown, "Predicting the Spinel-Nepheline Liquidus for Application to Nuclear Waste Glass Processing. Part II: Quasicrystalline Freezing Point Depression Model," *Journal of the American Ceramic Society* 90, no. 6 (2007): 1880–1891, https://doi.org/10.1111/j.1551-2916.2006.01028.x.

72. D. G. Casler and P. Hrma, "Nonisothermal Kinetics of Spinel Crystallization in a HLW Glass," *MRS Online Proceedings Library (OPL)* 556 (1999): 255–262, https://doi.org/10.1557/PROC-556-2.

73. M. Lasocka, "The Effect of Scanning Rate on Glass Transition Temperature of Splat-Cooled Te85Ge15," *Materials Science and Engineering* 23, no. 2–3 (1976): 173–177, https://doi.org/10.1016/0025-5416(76)90189-0.

74. H. E. Kissinger, "Reaction Kinetics in Differential Thermal Analysis," *Analytical Chemistry* 29, no. 11 (1957): 1702–1706, https://doi.org/10.1021/ac60131a045.

75. A. A. S. Lopes, R. C. C. Monteiro, R. S. Soares, M. M. R. A. Lima, and M. H. V. Fernandes, "Crystallization Kinetics of a Barium-Zinc Borosilicate Glass by a Non-Isothermal Method," *Journal of Alloys and Compounds* 591 (2014): 268–274, https://doi.org/10.1016/j.jallcom.2013.12.086.

76. J. M. Tainio, T. Anttila, J. Pohjola, D. S. Brauer, and J. Massera, "Crystallization Mechanism of B12.5 Bioactive Borosilicate Glasses and Its Impact on In Vitro Degradation," *Journal of the European Ceramic Society* 44, no. 2 (2024): 1229–1238, https://doi.org/10.1016/j.jeurceramsoc.2023.09.043.

77. H. Zhu, F. Wang, Q. Liao, D. Liu, and Y. Zhu, "Structure Features, Crystallization Kinetics and Water Resistance of Borosilicate Glasses Doped With CeO_2," *Journal of Non-Crystalline Solids* 518 (May 2019): 57–65, https://doi.org/10.1016/j.jnoncrysol.2019.04.044.

78. M. Avrami, "Kinetics of Phase Change. I: General Theory," *Journal of Chemical Physics* 7, no. 12 (1939): 1103–1112, https://doi.org/10.1063/1.1750380.

79. M. Avrami, "Kinetics of Phase Change. II Transformation-Time Relations for Random Distribution of Nuclei," *Journal of Chemical Physics* 8, no. 2 (1940): 212–224, https://doi.org/10.1063/1.1750631.

80. M. Avrami, "Granulation, Phase Change, and Microstructure Kinetics of Phase Change. III," *Journal of Chemical Physics* 9, no. 2 (1941): 177–184, https://doi.org/10.1063/1.1750872.

81. H. L. Giles, P. W. Hurley, and H. W. M. Webster, "Simple Approach to the Analysis of Oxides, Silicates and Carbonates Using X-Ray Fluorescence Spectrometry," *X-Ray Spectrometry* 24, no. 4 (July 1995): 205–218, https://doi.org/10.1002/xrs.1300240411.

82. A. Goncharov and S. Zhutovsky, "Comparison of Different Approaches for Quantification of Amorphous Phase in Hydrated Cement Paste by XRD", International RILEM Conference on Synergising Expertise towards Sustainability and Robustness of Cement-based Materials and Concrete Structures Conference paper (2023): 449–459, https://doi.org/10.1007/978-3-031-33211-1_40.

83. J. P. Cline, M. H. Mendenhall, D. R. Black, A. Henins, and J. B. Prothero, "Certification of Standard Reference Material® 640g," (NIST Special Publication 260, February 2024), https://doi.org/10.6028/NIST.SP.260-245.

84. S. N. Kabekkodu, A. Dosen, and T. N. Blanton, "PDF-5+: A Comprehensive Powder Diffraction File™ for Materials Characterization," *Powder Diffraction* 39, no. 2 (2024): 47–59, https://doi.org/10.1017/S0885715624000150.

85. R. Dimitrijevic, V. Dondur, P. Vulic, S. Markovic, and S. Macura, "Structural Characterization of Pure Na-Nephelines Synthesized by Zeolite Conversion Route," *Journal of Physics and Chemistry of Solids* 65, no. 10 (2004): 1623–1633, https://doi.org/10.1016/j.jpcs.2004.03.005.

86. P. Vulic, V. Kahlenberg, and J. Konzett, "On the Existence of a Na-Deficient Monoclinic Trinepheline With Composition $Na_{7.85}Al_{7.85}Si_{8.15}O_{32}$," *American Mineralogist* 93, no. 7 (July 2008): 1072–1079, https://doi.org/10.2138/am.2008.2702.

87. Y. Chen, S. Manna, B. Narayanan, Z. Wang, I. E. Reimanis, and C. V. Ciobanu, "Pressure-Induced Phase Transformation in β-Eucryptite: An X-Ray Diffraction and Density Functional Theory Study," *Scripta Materialia* 122 (September 2016): 64–67, https://doi.org/10.1016/j.scriptamat.2016.05.005.

88. J. S. McCloy and J. D. Vienna, "Glass Composition Constraint Recommendations for Use in Life-Cycle Mission Modeling," Richland, WA (United States) (Pacific Northwest National Laboratory, May 2010), https://doi.org/10.2172/978973.

89. B. H. Toby, "R Factors in Rietveld Analysis : How Good Is Good Enough ?," *Powder Diffraction* 21 (January 2006): 67–70, https://doi.org/10.1154/1.2179804.

90. B. Birajdar, N. Peranio, and O. Eibl, "Quantitative Boron-Analysis Using EDX in SEM and TEM," *Microscopy and Microanalysis* 13, no. S03 (2007): 290–291, https://doi.org/10.1017/S1431927607081457.

91. H. Shin, "An Study on the Structure of Maghemite(γ-Fe2O3) I. Rietveld Analysis of Powder XRD," *Journal of the Korean Ceramic Society* 35, no. 10 (1998): 1113–1119, https://koreascience.or.kr/article/JAKO199811920042309.page.

92. M. Ahmadzadeh, J. Marcial, and J. McCloy, "Crystallization of Iron-Containing Sodium Aluminosilicate Glasses in the $NaAlSiO_4$-$NaFeSiO_4$ Join," *Journal of Geophysical Research, Solid Earth* 122, no. 4 (2017): 2504–2524, https://doi.org/10.1002/2016JB013661.

93. M. Ahmadzadeh, A. Scrimshire, P. A. Bingham, A. Goel, and J. S. McCloy, "Structural Role of Iron in Nepheline-Based Aluminosilicates for Nuclear Waste Applications 18192," in *WM2018 Conference* (WM Symposia, June 2018).

94. P. Hrma, P. Schill, and L. Nemec, "Settling of Spinel in a High-Level Waste Glass Melter," (Pacific Northwest National Laboratory, 2002).

95. K. Lakshmi Narayan, K. Kelton, and C. Ray, "Effect of Pt Doping on Nucleation and Crystallization in Li_2O $2SiO_2$ Glass: Experimental Measurements and Computer Modeling," *Journal of Non-Crystalline Solids* 195, no. 1–2 (1996): 148–157, https://doi.org/10.1016/0022-3093(95)00526-9.

96. J. E. Shelby, *Introduction to Glass Science and Technology*, 2nd ed. (The Royal Society of Chemistry, 2020), https://doi.org/10.1039/9781839169229.

97. A. Kruger, R. L. Russell, B. P. McCarthy, et al., "Enhanced Hanford Low-Activity Waste Glass Property Data Development: Phase 2," technical report (Pacific Northwest National Laboratory, April 2021), https://doi.org/10.2172/1874932.

98. R. Russell, T. Jin, B. P. McCarthy, et al., "Enhanced Hanford Low-Activity Waste Glass Property Data Development: Phase 1," PNNL-26630 Rev 0 (Pacific Northwest National Laboratory, 2017), http://www.pnnl.gov/main/publications/external/technical_reports/PNNL-26630Rev0.pdf.

99. R. L. Russell, "Hanford Low-Activity Waste Glass Minor Component Concentration Boundary Expansion November 2022," (Pacific Northwest National Laboratory, 2022).

100. C. E. Lonergan, J. L. George, D. A. Cutforth, et al., "Enhanced Hanford Low-Activity Waste Glass Property Data Development : Phase 3," (Pacific Northwest National Laboratory, 2020).

101. I. Muller, I. L. Pegg, D. McKeown, et al., "LAW Glass Formulation to Support AZ-102 Actual Waste Testing," Final Report, Rev. 0 (Pacific Northwest National Laboratory, August 2003), https://doi.org/10.2172/1515181.

102. J. D. Vienna and J. V. Crum, "Non-Linear Effects of Alumina Concentration on Product Consistency Test Response of Waste Glasses," *Journal of Nuclear Materials* 511 (2018): 396–405, https://doi.org/10.1016/j.jnucmat.2018.09.040.

103. J. L. George, P. Ferkl, J. Marcial, T. Jin, P. Hrma, and A. A. Kruger, "Glass Transition Temperature of Low-Activity Waste Nuclear Glasses," *International Journal of Applied Glass Science (IJAGS)* 14, no. 3 (2023): 399–407, https://doi.org/10.1111/ijag.16629.

104. J. B. Hanni, E. Pressly, J. V. Crum, et al., "Liquidus Temperature Measurements for Modeling Oxide Glass Systems Relevant to Nuclear Waste Vitrification," *Journal of Materials Research* 20, no. 12 (2005): 3346–3357, https://doi.org/10.1557/jmr.2005.0424.

105. A. Heredia-Langner, V. Gervasio, S. K. Cooley, et al., "Hanford Low-Activity Waste Glass Composition-Temperature-Melt Viscosity Relationships," *International Journal of Applied Glass Science (IJAGS)* 13, no. 4 (2022): 514–525, https://doi.org/10.1111/ijag.16580.

106. X. Lu, I. Sargin, and J. D. Vienna, "Predicting Nepheline Precipitation in Waste Glasses Using Ternary Submixture Model and Machine Learning," *Journal of the American Ceramic Society* 104, no. 11 (2021): 5636–5647, https://doi.org/10.1111/jace.17983.

107. B. J. Riley, P. R. Hrma, J. D. Vienna, et al., "The Liquidus Temperature of Nuclear Waste Glasses: An International Round-Robin Study," *International Journal of Applied Glass Science (IJAGS)* 2, no. 4 (2011): 321–333, https://doi.org/10.1111/j.2041-1294.2011.00063.x.

108. S. V. Raman, "Microstructures and Leach Rates of Glass-Ceramic Nuclear Waste Forms Developed by Partial Vitrification in a Hot Isostatic Press," *Journal of Materials Science* 33, no. 7 (1998), https://doi.org/10.1023/A:1004313623562.

109. M. Martín, F. Andreola, L. Barbieri, et al., "Crystallisation and Microstructure of Nepheline–Forsterite Glass-Ceramics," *Ceramics International* 39, no. 3 (2013): 2955–2966, https://doi.org/10.1016/j.ceramint.2012.09.072.

110. M. R. Schroeder, *Fractals, Chaos, Power Laws: Minutes From an Infinite Paradise* (W. H. Freeman, 1991), https://doi.org/10.2307/3619149.

Supporting Information

Additional supporting information can be found online in the Supporting Information section.

Supporting File: ijag70034-sup-0001-SuppMat.docx.